CHALMERS
UNIVERSITY OF TECHNOLOGY

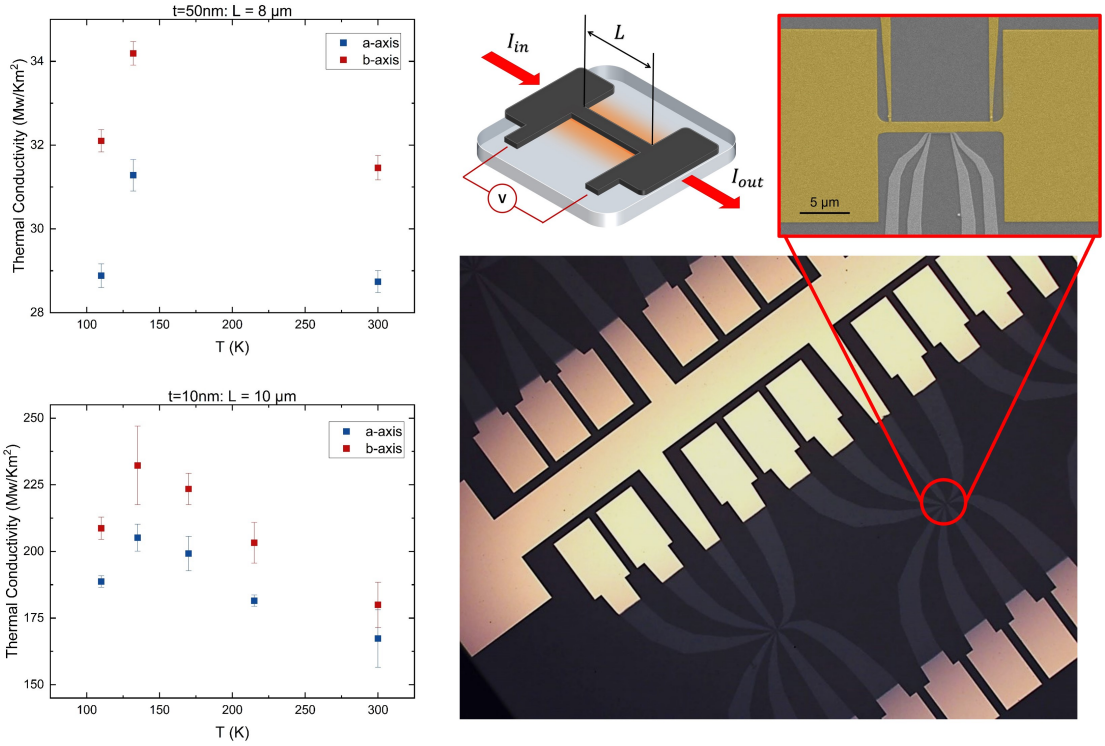

Probing electronic nematicity and anisotropic electron-phonon coupling in strained YBCO nanowires

Master's thesis in Nanotechnology

KARN RONGRUEANGKUL

DEPARTMENT OF MICROTECHNOLOGY AND NANOSCIENCE
CHALMERS UNIVERSITY OF TECHNOLOGY
Gothenburg, Sweden 2024
www.chalmers.se

Master's thesis 2024

Probing electronic nematicity and anisotropic electron-phonon coupling in strained YBCO nanowires

KARN RONGRUEANGKUL

CHALMERS
UNIVERSITY OF TECHNOLOGY

Department of Microtechnology and Nanoscience
Division of Quantum Device Physics
Quantum Materials and Nanodevices (QManD)
Chalmers University of Technology
Gothenburg, Sweden 2024

Probing electronic nematicity and anisotropic electron-phonon coupling in strained YBCO nanowires

KARN RONGRUEANGKUL

© KARN RONGRUEANGKUL, 2024.

Supervisor: Alexei Kalaboukhov and Thilo Bauch, Department of Microtechnology and Nanoscience
Examiner: Floriana Lombardi, Department of Microtechnology and Nanoscience

Master's Thesis 2024
Department of Microtechnology and Nanoscience
Division of Quantum Device Physics
Quantum Materials and Nanodevices (QManD)
Chalmers University of Technology
SE-412 96 Gothenburg
Telephone +46 31 772 1000

Cover: The image shows a large and small image of the design. The sketch shows the heating effect in the nanowire due to electrical power. The plots on the left-hand side are two of the key experimental results, which depict the heat transfer behaviours of the thick (50 nm) and ultrathin (10 nm) YBCO nanowires aligning along different in-plane crystallographic directions.

Typeset in LaTeX
Printed by Chalmers Reproservice
Gothenburg, Sweden 2024

Probing electronic nematicity and anisotropic electron-phonon coupling in strained YBCO nanowires

KARN RONGRUEANGKUL
Department of Microtechnology and Nanoscience
Chalmers University of Technology

Abstract

Despite nearly 40 years since its discovery in 1986, the underlying mechanism behind the high-temperature superconductivity (HTS) in cuprates remains a significant enigma in condensed matter physics. The existence of multiple intertwined local orders, originating from the strongly correlated electrons, further complicates the study of these materials. Such complexity of the normal state is depicted in a very intricate temperature-doping phase diagram. A way to advance the knowledge of these materials is to tune the local orders, both in the superconducting and in the normal state, to disentangle them for individual study. One way to achieve such an effect is to apply strain to the cuprates in nm-thick films. Previously, it was discovered that the unidirectional strain, induced by few-unit-cell-thick films deposited on a nanostructured surface, can modify the charge order and cause the in-plane resistivity of the films to become much more anisotropic than in bulk materials. According to the Boltzmann transport model, such anisotropy in the in-plane resistivity is due to the directional modification of the Fermi velocity in which the velocity along one crystallographic in-plane direction is much higher than another. This results in an anisotropic Fermi surface that connects to the presence of an electronic nematicity, wherein the electronic structure retains translational symmetry while spontaneously breaking rotational symmetry.

In earlier reports on the archetypal HTS $YBa_2Cu_3O_{7-\delta}$ (YBCO) superconductor, the photoemission and transport measurements appear to show that electron-phonon coupling (EPC) can become directionally suppressed if the Fermi surface becomes nematic (as in our sample). This should strongly affect the heat transport in nm-thick YBCO films. Hence, the focus of this thesis work is to investigate the anisotropic EPC through the study of electrical and heat transport properties of YBCO nanowires oriented along different crystallographic axes. The nanowires are fabricated from YBCO thin films epitaxially grown by the Pulsed Laser Deposition technique, and the strain is tuned by modifying the film thickness.

Keywords: High-Temperature Superconductors, YBCO, Electronic Nematicity.

Acknowledgements

First and foremost, I am expressing my deepest gratitude to Floriana Lombardi who warmly welcomed me into the group and provided me with an opportunity to work on such a fascinating topic that sparked my deep interest in pursuing the academic field. I cherished the time I spent in a group that was full of brilliant and amazing individuals.

My thesis journey would not have been possible without Thilo Bauch, who endlessly supported and guided me in the measurement lab from the beginning until the end. I also deeply appreciate the brilliant and knowledgeable insights that you provided during our discussions. I am also extending my sincere gratitude to Alexei Kalaboukhov for his help and guidance in operating deposition and characterization tools. You also provided me with important skills that helped me with my journey to become a better experimentalist.

I would like to express my deep gratitude to Eric Wahlberg, who initially supervised me and guided me a lot from the deposition to characterization tools. Beyond the technical skills, you taught me a lot about the knowledge important for data analysis, and you were always welcome to guide me when I had some doubts. I am expressing my deep gratitude to Riccardo Arpaia as well. Although I did not get a chance to work directly with you during my thesis work, you are always welcome to guide me throughout my journey. I also deeply appreciate the time you supervised me during the summer. The summer tasks were very interesting and I learned a lot from you beyond the scope of my thesis. I am grateful that I get a chance to work with a great researcher like you.

Moreover, I am expressing my special thanks to Núria Alcalde-Herraiz who guided and assisted me with the lab, especially the nanofabrication processes. I greatly appreciate your kindness and your willingness to supervise me throughout my thesis work. I am also extending my special thanks to other members of the group who helped me at some points along my journey. Everyone has been incredibly nice to me, and I consider myself fortunate to have the opportunity to work in this amazing group.

Finally, I want to extend my heartfelt thanks to my parents, who have been my unwavering support for as long as I can recall. Even during the hardest time, both of you were willing to support me without hesitation. I also would like to express my deep gratitude to my grandmother who also financially supported me during my master's study. A special shout-out goes to my twin brother (a.k.a. my best bro), for being an unwavering pillar of support during both the good times and the challenging moments. I would never made it this far without all of your support.

Karn Rongrueangkul, Gothenburg, September 2023

List of Acronyms

Below is the list of acronyms that have been used throughout this thesis listed in alphabetical order:

AF	Antiferromagnetic
ARPES	Angle-resolved photoemission spectroscopy
BCS	Bardeen–Cooper–Schrieffer
BSCCO/Bi2212	$Bi_2Sr_2CaCu_2O_{8+x}$
C_4	Four-fold rotational symmetry
CDW	Charge Density Wave
$d_{x^2-y^2}$	d-Wave Order Parameter
e-ph	Electron-Phonon Coupling
HTS	High-Temperature Superconductivity
LBCO	$La_{2-x}Ba_xCuO_4$
LSCO	$La_{2-x}Sr_xCuO_4$
PLD	Pulsed laser deposition
RIXS	Resonant Inelastic X-ray Scattering
SEM	Scanning Electron Microscope
STM	Scanning Tunning Microscope
YBCO	$YBa_2Cu_3O_{7-\delta}$

Parameters

Δ	Superconducting Energy Gap
ΔT_c	A parameter that shows the broadening of the superconducting transition
B_c	Critical Magnetic Field
J_s	Supercurrent Density
k_b	Boltzmann constant
l_{e-ph}	Electron-phonon scattering length
l_0	Thermal relaxation length
n_s	Superconducting Electron Density
T_{ph}	Phonon Temperature
T_c	Critical Temperature
T_c^{on}	Onset of the superconducting transition
T_e	Electron temperature
Λ	London Parameter
λ_L	London Penetration Depth
μ_0	Vacuum permeability
ξ	coherence length
ψ	Order Parameter
ω_D	Debye Frequency

Contents

List of Figures

List of Tables

1
Introduction

A significant breakthrough in superconductivity research happened when the first high-temperature superconductor (HTS) was discovered in 1986 [1], with a critical temperature (T_c) above 30 K. This remarkable breakthrough defied the expectations set by the well-established Bardeen–Cooper–Schrieffer (BCS) theory, which beautifully describes conventional superconductivity phenomena [2]. The material that is responsible for this breakthrough belongs to the family of ceramic copper-oxide, commonly referred to as 'cuprate'. This discovery inspired an intense scientific pursuit, driven by the quest for cuprate-based HTS materials with even higher T_c values [3, 4]. The ultimate aim is to discover the room-temperature superconductor, which will have a tremendous impact on technological advancement. So far, the incomplete understanding of the underlying mechanism of HTS has prevented us from fully utilizing HTS materials to their potential.

The microscopic origins of HTS have posed one of the most perplexing mysteries in the field of condensed matter physics. This is due to the strongly correlated electrons nature of the materials [5, 6], in which the single-particle picture breaks down. For almost 40 years, theoretical models have been attempted to unravel the microscopic origins of HTS [7–13], but none have been able to comprehensively capture their complexity. Beyond the unconventional superconductivity, the normal state of the HTS cuprates is even more enigmatic. Due to the strong electron-electron correlations, intertwined spin/charge orders exist beyond superconductivity in cuprates, leading to a complex electronic phase diagram [6], which adds another level of complexity to the study of HTS. Although the origins of the local orders are not completely understood, theoretical reports have linked them to the superconducting order [14]. The strange metallicity, which is characterized by T-linear resistivity and Planckian dissipation (carrier scattering time approaches the fundamental threshold), adds yet another layer of complexity. The holographic model, based on the string theory, suggested that the strange metal phase originated from the formation of densely entangled quantum matter, or a 'soup' of entangled electrons [15]. Interestingly, there is evidence that hints towards a fundamental link between HTS and strange metallicity [16]. Hence, understanding this enigmatic phase, along with local orders, would be the key step to unraveling the secret of the HTS.

The complexity of HTS cuprates makes it difficult to study their effects at the microscopic level. Possible ways to advance the knowledge are to remove the superconductivity [17] or to tune the local orders [18, 19]. The work done in our group focuses on tuning local orders by applying strain to $YBa_2Cu_3O_{7-\delta}$ (YBCO), a cuprate HTS, in nm-thick films. Recently, it has been shown that unidirectional compressive strain, induced by the substrate with a nanostructured surface on few-unit-cell-thick films, dramatically modifies the resistivity of the films to become much more anisotropic than in bulk samples [20]. The charge order is suppressed along the crystallographic direction orthogonal to the applied strain, which results in the restoration of strange metallicity along one direction down to the superconducting critical temperature. For the anisotropic resistivity, a theoretical model points out that the anisotropy in transport measurement could originate from an anisotropic Fermi surface caused by the unidirectional strain. This signals the presence of an electronic nematicity, a phase where the electronic states order themselves in a preferred direction, with potential implications for superconductivity [14]. The presence of this nematic phase can persist from the underdoped to the optimally doped region. The presence of an anisotropic Fermi surface would result in **electron-phonon coupling (e-ph coupling)** along the in-plane crystallographic axes [21]. The suppression of e-ph coupling should be reflected in anisotropic transport properties.

The goal of this thesis is to investigate the nematic phase through the study of electrical and heat transport properties of YBCO nanowires. Our primary strategy to highlight the anisotropy is to perform experiments on the nanowires that orient along different crystallographic directions, one of which is the direction where e-ph coupling should be suppressed. Since the strain can be tuned by changing the thickness of the thin film, two thicknesses were selected to compare the nanowires with and without the anisotropic Fermi surface.

The outline of the thesis is as follows:

- *Chapter 2* provides a brief overview of the history of superconductivity and HTS, properties of YBCO including its phase diagram, and evidence of nematic phase in cuprates including YBCO.
- *Chapter 3* explains the deposition of YBCO thin films, along with the characterization of structural and transport properties.
- *Chapter 4* provides a comprehensive overview of the nanofabrication process to pattern the YBCO nanowires.
- *Chapter 5* aims to provide the necessary information and theoretical framework to study electrical and heat transport in YBCO nanowires. The chapter also includes the nanowire design, simulation, and experimental setup.
- The results of the transport measurements are discussed in *Chapter 6*. The first half discusses the results for the 50 nm thick YBCO nanowires, while the second half shifts the focus to 10 nm nanowires, a thickness that displays anisotropic behaviours.
- The last chapter concludes the study and gives some outlook for future studies.

2

Background

This chapter aims to provide some historical and theoretical backgrounds that are important for the understanding of superconductivity. Afterward, the focus will be shifted towards an explanation of cuprate HTS, from properties to electronic phase diagram, that acts as necessary background for this thesis.

2.1 Historical Overview of Superconductivity

The field of superconductivity began in 1911 when H. K. Onnes measured the resistivity of mercury as a function of temperature with liquid helium [22]. In the experiment, Onnes discovered that the resistivity of mercury vanishes at 4.19 K. The transition temperature, where the materials become a perfect conductor, is known as 'Critical Temperature (T_c)'. These materials are later referred to as 'superconductors'.

The second distinctive characteristic of superconductors – a perfect diamagnetism - was discovered by W. Meissner and R. Ochsenfeld in 1933 [23]. They discovered that superconductors can expel external magnetic fields from their bulk when cooling below T_c. This phenomenon is known as the 'Meissner effect'. However, this effect breaks down when the applied magnetic field exceeds a critical value (B_c).

In 1935, the London brothers developed equations to describe the characteristics of superconductivity [24]. They proposed that electrons in superconductors are characterized by the two-fluid model, composed of superfluid (characterized by zero viscosity and entropy) and normal fluid. The main idea is that the superfluid part gives rise to the superconducting mechanism. By relating the superfluid to the electrodynamics of the superconductors, two London equations were established:

$$\vec{E} = \Lambda \frac{\partial}{\partial t} \vec{J}_s \tag{2.1}$$

$$\vec{B} = -\Lambda \nabla \times \vec{J}_s \tag{2.2}$$

where $\Lambda = \frac{m^*}{n_s e^{*2}}$ and J_s are London parameter and superconducting current, respectively. The mass (m^*), charge (e^*) and density (n_s) represent the superconducting electrons in which $m^* = 2m$ and $e^* = 2e$. The first equation describes the collisionless response of a superconducting fluid (perfect conductivity), where the free acceleration of the superfluid gives rise to the superconducting current J_s. The second equation is the first model that successfully describes the Meissner effect. By applying the curl of Ampere's law $\nabla \times \vec{B} = \mu_0 \vec{J}_s$, where μ_0 is the vacuum permeability, the second equation becomes

$$\Delta \vec{B} = \frac{1}{\lambda_L^2} \vec{B}, \qquad \lambda_L = \sqrt{\frac{\Lambda}{\mu_0}} \tag{2.3}$$

and its solution describes how the external magnetic field is completely screened from the bulk material by the supercurrent which flows in a thin layer on the surface of superconductors. The characteristic length describing how much the magnetic field can penetrate the superconductor is known as the London penetration depth (λ_L).

Although the London equations successfully describe two important characteristics of the superconductors, the first phenomenological theory to successfully describe the behaviours of superconductors was developed by V. L. Ginzburg and L. D. Landau in 1950 [25]. The Ginzburg-Landau theory was developed based on Landau's theory of second-order transition proposed in the early 1940s, as the free energy description of superconductors aligns with the general theory of second-order phase transition. In the publication, Ginzburg and Landau introduced the order parameter, ψ, that represents the 'superfluid' part. The order parameter is assumed to be a 'plane wave', with $\varphi(r) = |\psi(r)| e^{i\theta}$ and $n_s = |\psi(r)|^2$. Since the theory was developed close to the transition temperature, where $|\varphi(r)|$ and its gradient is assumed to be small, the free energy takes the form of a field theory:

$$F = F_N + \int \left[\alpha |\psi|^2 + \frac{1}{2}\beta |\psi|^4 + \frac{1}{2m} \left| \left(-i\hbar\vec{\nabla} - e^* \vec{A} \right) \psi \right|^2 + \frac{1}{2\mu_0} |B|^2 \right] dV \tag{2.4}$$

where F_N is the free energy of the normal state, $\vec{A}$ is the vector potential, $\alpha = \frac{\partial F}{\partial n_s}$ and $\beta = \frac{\partial^2 F}{\partial n_s^2}$ are phenomenological parameters. The Ginzburg-Landau (GL) equations were obtained by minimizing the free energy with respect to a variation in order parameter (φ^*) and $\vec{A}$, which reads

$$\alpha\psi + \beta |\psi|^2 \psi + \frac{1}{2m} \left(-i\hbar\vec{\nabla} - e^* \vec{A} \right)^2 \psi = 0 \tag{2.5}$$

$$\vec{J_s} = -\frac{ie^*\hbar}{2m} \left(\psi^* \nabla\psi - \psi \nabla\psi^* \right) - \frac{e^{*2}}{m} |\psi|^2 \vec{A} \tag{2.6}$$

with a boundary condition $\left(-i\hbar\vec{\nabla}\psi - \frac{e}{c}\vec{A}\psi \right) \cdot \vec{n} = 0$ where $\vec{n}$ is the unit vector normal to the boundary. The boundary condition corresponds to $\vec{J_s} \cdot \vec{n} = 0$, meaning that the supercurrent cannot flow out of the superconductor. The second characteristic length, the coherence length or ξ, can be obtained by solving the first GL equation (2.5) by assuming that 1) the supercurrent phase θ always remains zero everywhere (constant superconducting electron density), 2) the magnetic field is negligible and 3) the order parameter is real but very small and slowly varying in space. By using these assumptions, equation (2.5) now becomes

$$\nabla^2\psi = \frac{\psi}{\xi^2}, \qquad \xi = \sqrt{\frac{\hbar^2}{2m|\alpha|}} \tag{2.7}$$

in which the coherence length (ξ) determines the distance of a spatial change in the order parameter. The ratio between the two characteristic lengths, $\kappa = \frac{\lambda}{\xi}$, determine whether the superconductor is type I ($\kappa < \frac{1}{\sqrt{2}}$) or type II ($\kappa > \frac{1}{\sqrt{2}}$). For type I superconductors, the interface between superconducting and normal regions is not energetically favorable. Hence, the material can completely expel the magnetic field only up to $B = B_c$. The situation is not the same as type II where the interface formation is favorable, as demonstrated by A. A Abrikosov in 1957 [26]. The materials expel the applied magnetic field similarly to type I up to the lower critical field $B = B_{C1}$. The magnetic field above

B_{C1} can enter the bulk in the form of vortices up to the upper critical field $B = B_{C2}$ where the whole superconductor becomes normal.

Besides GL theory, another important discovery also happened in 1950: the isotope effect. E. Maxwell [27] discovered that the critical temperature of mercury depends on the isotopic mass, coinciding with a theoretical prediction made independently by H. Fröhlich [28] and J. Bardeen [29] in the same year. According to the theoretical prediction, the T_C is proportional to the mass $M^{-1/2}$. Since the vibration frequencies show the same dependency on mass, the experiments signal the fundamental relations between **electron-phonon coupling (e-ph coupling)** and superconductivity.

In 1957, J. Bardeen, L. Cooper, and J.R. Schrieffer developed the first microscopic theory of superconductivity known as BCS Theory [30, 31]. The main 'ingredient' for the development of the BCS theory is the formation of electron pairs due to e-ph coupling. In 'bad' metals such as aluminum, the phonon-mediated electron-electron interaction can dominate over Coulomb repulsion which results in the net attractive force. This attractive force acts as a 'glue' for electrons with an opposite spin to pair up and form a singlet state known as **Cooper pairs**. The Cooper pairs are assumed to virtually form in the vicinity of the Fermi edge, and the pair formation is energetically favorable at $T < T_c$. Consequently, the density of states at the Fermi edge is approximated as a constant $N(\varepsilon_f) = N_0$. The matrix element of the electron-phonon interaction Hamiltonian is also assumed to be constant around the Fermi edge ($V_{kk'} = V_0$), otherwise becoming zero due to Pauli blocking.

The BCS theory predicts the binding energy of the Cooper pair with a value of 2Δ where Δ is a superconducting gap. The value of Δ can be calculated, through series of approximations, at zero temperature limit using $k_B T_c \approx 2\hbar\omega_D e^{-\frac{1}{N_0 V_0}}$ in the weak-interaction limit ($k_B T_c \ll \hbar\omega_D$) where k_B and ω_D are Boltzmann constant and Debye frequency, and $N_0 V_0$ represents the coupling parameter. Also, the T_c of superconductors can be approximated with $\Delta(0) = 1.76 k_B T_c$. Although BCS theory effectively explains the principles governing conventional superconductors, the highest critical temperature predicted by the theory is only 40K even in the strong interaction limit [32].

2.2 High T_C Superconductor and $YBa_2Cu_3O_{7-\delta}$

High-temperature superconductors (HTS) are unconventional superconductors that have a critical temperature higher than the theoretical values predicted by the BCS theory. Due to their complexity, the nature of the material has still been an ongoing research topic for nearly 40 years after their discovery. This section aims to provide some overview of the material before explaining the properties of a specific HTS called $YBa_2Cu_3O_{7-\delta}$ in detail.

2.2.1 Brief History and Roadmap of HTS

The first HTS was discovered by J. G. Bednorz and K. A. Müller in 1986 [1]. $La_{2-x}Ba_xCuO_4$ (LBCO), having a critical temperature of 35 K, belongs to a class of ceramic copper-oxide materials called "cuprate". The discovery was astonishing because not only does the T_c of LBCO surpass the theoretical limit predicted by the BCS theory, but cuprates are also ceramic materials that are typically associated with insulating properties. Less than a year after the discovery, a cuprate called $YBa_2Cu_3O_{7-\delta}$ (YBCO) with T_c 92 K was found [33]. This discovery is also significant since YBCO is the first superconductor that displays superconductivity just by using liquid nitrogen (77 K) which is much more economically suitable for real-world applications than using liquid helium. Since then, cuprates with higher and higher T_c under an ambient pressure were discovered, even reaching 135 K in a mercury-based compound in 1999 [6]. In addition, more classes of HTS materials besides cuprate have been discovered since the 2000s. **Figure 2.1** shows the roadmap of HTS since its discovery until recent years [4]. This thesis focuses on the study of **YBCO**, which is one of the most famous cuprates for fundamental studies and applications alongside $Bi_2Sr_2CaCu_2O_{8+x}$ (BSCCO or Bi2212) and $La_{2-x}Sr_xCuO_4$ (LSCO).

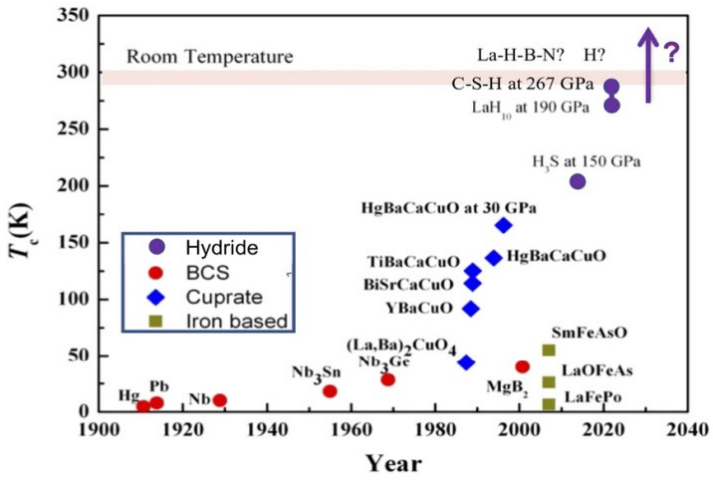

Figure 2.1: Roadmap of High-Temperature Superconductivity [4].

2.2.2 Structure and Properties of $YBa_2Cu_3O_{7-\delta}$

Cuprate HTS are characterized by a quasi-2D structure consisting of layers of CuO_2 planes separated by spacing layers. The structure can be described as a superlattice with unit cells resembling a defected perovskite structure. The CuO_2 planes are mainly responsible for the carrier transport and the superconducting properties of the material. Meanwhile, the spacing layers act as charge reservoirs for CuO_2 planes and maintain the cohesion of the whole atomic structure. The coupling between adjacent CuO_2 planes is weak due to spacing layers, resulting in a large anisotropy in the transport properties between in-plane and out-of-plane directions. In the case of YBCO, the structure consists of three perovskite layers: one cell with Yttrium in between two cells with Barium, as shown in **Figure 2.2** [34].

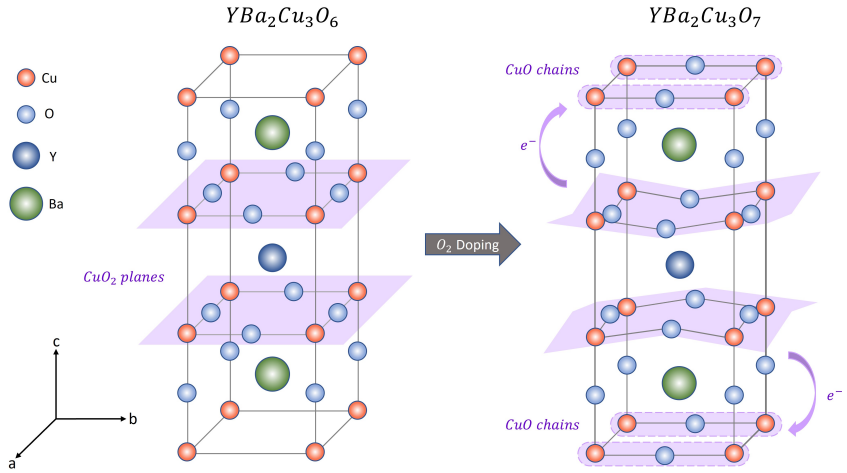

Figure 2.2: Illustration of YBCO crystal structure and the hole-doping mechanism (adapted from [34]). The parent compound ($YBa_2Cu_3O_6$) has a tetragonal structure with lattice parameters a=b=3.86 Å,c=11.82 Å. The formation of CuO chains from oxygen (hole) doping distorts the crystal structure, resulting in orthorhombic with lattice parameters a = 3.82 Å, b = 3.89Å, c = 11.68Å for the fully developed CuO chains.

The parent (undoped) compound, $YBa_2Cu_3O_6$, has a tetragonal structure with two oxygen-deficient layers containing only Cu atoms (the left structure of Figure 2.2). When introducing oxygen atoms into the structure, those atoms are bonded with Cu in the oxygen-deficient layer into quasi-1D CuO chains aligning along [010] direction (b-axis). The presence of the CuO chain transforms the crystal structure to orthorhombic with $b > a$ [35], which introduces anisotropy in YBCO properties. Due to the formation of CuO chains, the quasi-2D CuO_2 layers become slightly distorted, or "puckered". The c-axis length is also changed with the amount of doping, as observed in both single-crystal and thin-film YBCO [36–38]. The anisotropy in the transport properties of YBCO is reflected in anisotropic superconducting parameters, such as the penetration depth and coherence length, along the crystallographic axes. **Table 2.1** compares YBCO properties with conventional superconductors [39–41].

Material	SC Type	$T_C(K)$	Δ(meV)	$\lambda^a;\lambda^b;\lambda^c(nm)$	$\xi^{ab};\xi^c$(nm)	$B_c/B_{C2}(T)$
Al	1	1.175	0.18	50	1600	0.01
Pb	I	7.19	1.32	39	83	0.08
In	I	3.405	0.52	64	440	0.028
Nb	II	9.25	1.5	44	40	~ 3.5
$YBa_2Cu_3O_{6.9}$	II	93	$20-25$	$150-300;\lambda^a/1.2;$ $\sim 1,000$	$1-3;\sim 0.24$	120

Table 2.1: Comparison of superconducting properties of optimally doped YBCO to some conventional superconductors.

2.2.3 Order Parameter, Fermi surface and Electron-Phonon Coupling in Cuprates

While conventional superconductors have order parameters with s-wave symmetry (**Figure 2.3(a)**), cuprates' order parameters take the form of $d_{x^2-y^2}$ symmetry (also known as d-wave) (**Figure 2.3(b)**) [42]. Unlike the energy gap (Δ) of the s-wave order parameter that varies isotropically in the k-space, the Δ of the d-wave order varies according to $\Delta_d(k) = \Delta_0(\cos k_x - \cos k_y)$. The four lobes of the $\Delta_d(k)$ align orthogonally along the a and b crystallographic directions. The corresponding (simplified) Fermi surface is shown in **Figure 2.3(c)** and **Figure 2.3(d)**. Typically for cuprates, the Fermi surface is assumed to be a large hole-like cylinder that centers at the (π, π) point in the first Brillouin zone. The Fermi surface is mostly gapped at the 'anti-nodal' region, which corresponds to $(0, \pm\pi)$ and $(\pm\pi, 0)$ as shown in the figure. These are the points where the lobes of the $\Delta_d(k)$ are maximized. The 'nodal' region corresponds to the point where the superconducting gap is minimized. However, the topology of the Fermi surface can be modified, for example, by changing the oxygen content which will be further explained in the next section. (It is noted that the complete version of the Fermi surface has to include a contribution of bi-layer splitting (bonding vs anti-bonding bands) and CuO chain [43].)

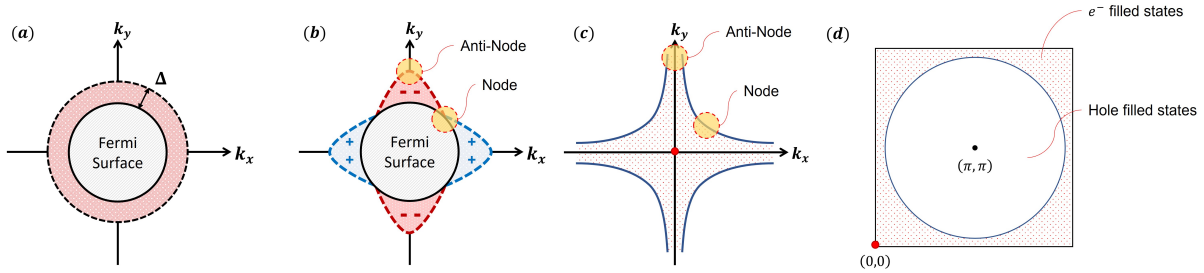

Figure 2.3: Illustration of (a) s-wave order parameter, (b) d-wave order parameter. Both (c) and (d) are the sketch of the Fermi surface where (c) is centered at (0,0) and (d) is centered at the (pi, pi) point of the first Brillouin zone

When looking from the perspective of the BSC theory, it seems that e-ph coupling should play a minor role in the electron pairing mechanism in HTS. However, experimental and theoretical studies (e.g., from angle-resolved photoemission spectroscopy (ARPES) [44, 45], Resonant Inelastic X-ray Scattering (RIXS) [46], and Raman Spectroscopy [47]) suggested that electron-phonon coupling also plays an important role in

both superconducting and normal state. There are three important phonon modes in cuprates including YBCO [47–49]: 1) Bond Buckling mode (A_{1_g} and B_{1_g}), where oxygen atoms in CuO_2 planes vibrate along the c-axis in alternating fashion causing the bonding between Cu and O to become buckled, 2) bond stretching mode or breathing phonon where oxygen, in the CuO_2 planes vibrate in-plane against Cu atoms causing the structure to elongate /compress (hence the name 'breathing'), and 3) Apical Oxygen mode, where oxygen atoms above/below CuO_2 planes vibrate along the c-axis in the opposite direction. When considering all phonon modes, it has been both theoretically and experimentally confirmed that the strength of e-ph coupling is stronger in the anti-nodal region than in the nodal area (e.g., see **Figure 2.4**). Hence, the e-ph coupling is most substantial along the crystallographic direction where the superconducting gap is also maximized (**Figure 2.3**). In addition, a connection between e-ph coupling strength and T_c was discovered [46, 50–52], and theoretical calculations reveal that the e-ph coupling could be involved in the formation of some local orders order [53, 54] in the materials. However, further investigation is required to figure out the exact role of the e-ph coupling in cuprate HTS.

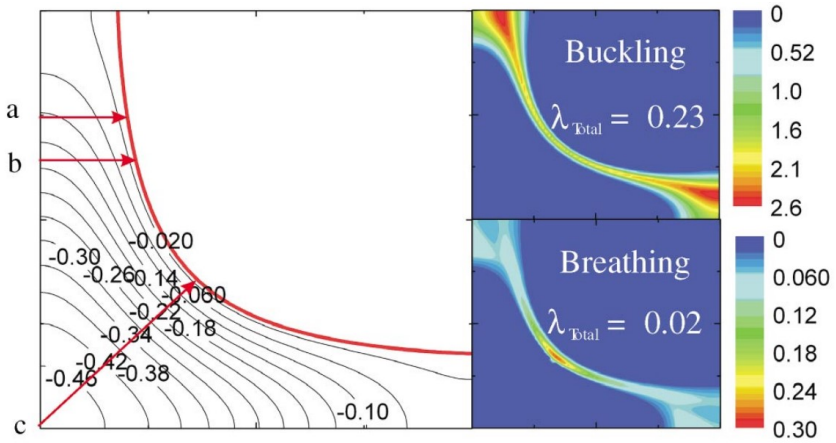

Figure 2.4: Plot of the effective e-ph coupling in the first quadrant of the Brillouin zone [44], where the colour scale shows the strength of e-ph coupling. Overall, the electronic states couple strongly with the phonon modes in the anti-nodal region.

2.2.4 Phase Diagram of YBCO

The properties of YBCO can be tuned with the amount of oxygen doping (p) to the CuO chains. The different amounts of doping and the complex nature of YBCO results in an intricate phase diagram as shown in **Figure2.5**. The superconductivity of YBCO spans from $0.05 < p < 0.23$ and the critical temperature maximizes at p=0.16 with $T_c \sim 93K$. In YBCO, the trend of the critical temperature deviates from a superconducting 'parabolic dome', where the suppression is maximized at $p \sim 0.125$ which is typically called 1/8 anomaly. The suppression of T_c is typical among the cuprates [55], and the suppression could be a consequence of a competition between superconductivity and charge order (more details below). Hole doping can be divided into three distinct regions: underdoped, optimally doped, and overdoped.

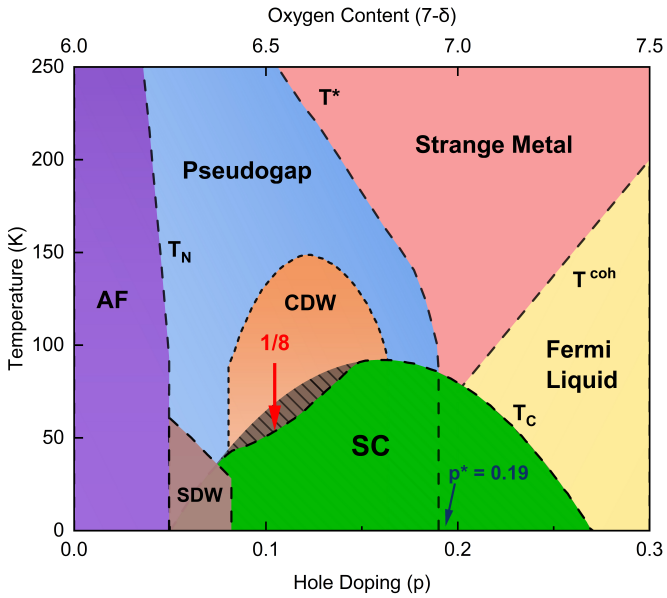

Figure 2.5: Phase diagram of YBCO as a function of hole doping (p) and oxygen content ($7-\delta$) per unit cell (adapted from [34]). YBCO is characterized by multiple intertwined orders, depending on the level of doping as shown in the diagram. T_N, T^*, and T_{coh} are Néel, Pseudogap, and coherent temperature, respectively.

2.2.4.1 The Underdoped Region ($p < 0.16$)

The underdoped region is the most complex part of the phase diagram where multiple spin/charge orders are intertwined. This section explains the normal state existing in the underdoped region starting from undoped YBCO:

- **Mott Insulator**: Around zero doping, YBCO is a Mott insulator with one hole per Cu site (half-filled) that displays antiferromagnetic (AF) order [56]. The carriers are strongly bounded due to strong on-site Coulomb interaction, so the compound becomes an insulator instead of metallic according to the band theory. The AF phase can be easily destroyed by introducing hole doping ($p \sim 0.05$) to the lattice causing holes to become less localized.
- **Spin Order**: The spin order in the form of Spin Density Wave (SDW), a periodic modulation of electron spins, exists immediately after the end of the AF phase in the doping range of $0.05 < p < 0.08$ [57]. In YBCO, the spin order does not overlap much with the charge order which differs from other cuprates as LSCO [58–60].
- **Pseudogap**: A phase known as pseudogap dominates a large part in the underdoped region of the phase diagram. Pseudogap is a region where states are partially depleted from the Fermi surface along the anti-nodal directions. As a consequence, the Fermi surface takes the form of 'Fermi Arcs' (**Figure2.6(a)**) instead of a hole-like cylinder (**Figure 2.3(c)**) [61–63]. The pseudogap phase has two important parameters, which are the critical doping (p^*), where the pseudogap phase abruptly ends, and the onset temperature (T^*). For YBCO, p^* is at $p = 0.19$ [64]. Above this point, the normal Fermi liquid behaviour is restored. The T^* is normally evidenced by the formation of the Fermi arc (e.g., see [65]). For YBCO, the data on photoemission is lacking so the T^* is defined as the temperature where $\rho(T)$ deviates from linearity [66].

The interplay between pseudogap and superconductivity is still under debate. On the one hand, pseudogap and superconducting order seem to compete with each other, indicated by the fact that the Fermi arcs vanish near the nodal region of the Fermi surface when approaching T_c (where d-wave superconducting order emerges) [67]. However, other evidence showed that pseudogap might be a precursor to the superconducting order since both orders are linked through spin/pairing fluctuation [68, 69]. The only possible conclusion is that the pseudogap and superconductivity are two distinct orders [70]. The pseudogap phase, along with strange metallicity, remains the top mystery in the topic of HTS.

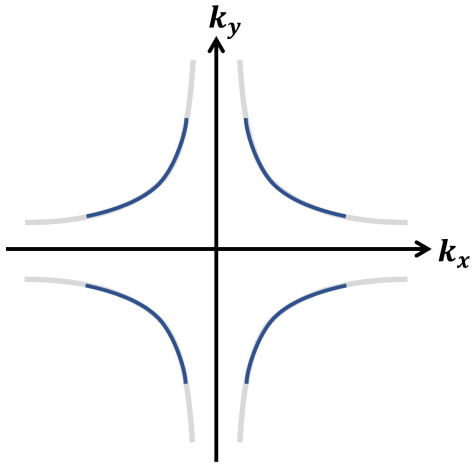

Figure 2.6: Simplified illustration of the Fermi surface of the pseudogap phase (Fermi Arc). The grey lines denote the Fermi surface of the normal hole-like cylinder.

- **Charge Order**: A charge order in the form of Charge Density Wave (CDW) exists in a large part of the underdoped region, covering the doping range of $0.08<p<0.16$. Generally, CDW in cuprate HTS is a modulation of conducting electrons (charges) density in the CuO_2 plane, which is incommensurate with the in-plane lattice parameters. The onset temperature of CDW is doping dependent, and it peaks near p 1/8, while the range of this temperature lies between the critical temperature and T^*. For YBCO, the charge order is a short-ranged and quasi-2D biaxial CDW with an in-plane correlation length of at most $\sim$ 75Å (20 lattice constant) [71, 72]. The results from resonance x-ray scattering of YBCO revealed anisotropy in charge modulation along the in-plane direction, which maximizes near $p \sim 1/8$ [73]. This anisotropic CDW breaks the four-fold (C_4) rotation symmetry. Although the CDW has not been completely understood, there is evidence pointing toward the competition between CDW and superconductivity [71, 72]. For instance, the strength of CDW increases when approaching T_c from high temperature but decreases below the superconducting state. Also, the intensity of CDW is maximized at $p \sim 1/8$ where superconductivity is suppressed the most.

2.2.4.2 The Optimally Doped Region ($p = 0.16$)

The optimally doped region is where the critical temperature is maximized and the normal state is mainly characterized by a 'strange metal phase', which is considered one of the most mysterious features in the HTS materials. At first glance, the trend of the $\rho(T)$ looks very simple: just a perfectly straight line from millikelvins [74] up to above a thousand kelvin [75] (only when superconductivity is removed by applying magnetic field). According to the Fermi liquid model, which is based on a quasiparticle picture of the electron gas [76], the $\rho(T)$ for normal metals follows complex power lats (e.g., starts with T^2 then follows by T^5 at low temperature due to the electron-electron and electron-phonon scattering. The trend instead shows saturation at high temperatures because the mean free path of electrons becomes comparable to the inter-atomic spacing (known as the Mott-Ioffe-Regel limit [77]). Then, it is obvious that the microscopic behaviour of the strange metal deviates from the typical Fermi liquid in normal metals.

Aside from the deviation of $\rho(T)$ from the Fermi liquid behavior, the strange metal phase also exhibits a fascinating anomaly: the disappearance of quasiparticles [65, 78]. The unparticle nature strongly reinforces the departure from the Fermi liquid model. Another key feature of the strange metal is the carrier scattering time which takes values approximately equal to the fundamental limit known as 'Planckian dissipation' or $\tau_p = \hbar/k_B T$ [15]. When approaching this limit, the carrier scattering rate is extremely fast so that the quasiparticle picture breaks down. These properties seem to be universal among cuprates [79].

The origin of the strange metal remains an enigma in the field of condensed matter physics. One hypothesis suggests that the strange metallicity could emerge from a quantum critical point, a phase transition at the $T = 0$ and $p = p^*$ that is governed by quantum fluctuation instead of thermal fluctuation [80, 81]. While the exact connection between the quantum critical point and strange metallicity is still not established, recent studies suggest a potential link to the charge density fluctuations, a charge modulation with correlation length shorter than CDW but persisting up to room temperature, and therefore pervasive in the strange metal region [82–84].

On the other hand, the Planckian dissipation and a loss of quasiparticle nature in strange metal suggests that carriers form a novel state of matter referred to as 'densely many-body entangled quantum matter' [15]. In this scenario, countless carriers are entangled with each other, resembling a 'soup of entanglement'. The theoretical framework used to develop this concept is known as the holographic model, which is based on string theory. Aside from being able to explain properties such as T-linear resistivity and Planckian dissipation, it also reveals that the behaviour of strange metals is governed by the law of hydrodynamics. This prediction is also valid in other strongly correlated materials, such as Kagome metals [85]. Nevertheless, it is important to note that there is currently no experimental confirmation of the hydrodynamic nature (e.g., turbulent flow) of strange metal in cuprates.

2.2.4.3 The Overdoped Region ($p > 0.16$)

The overdoped region is less complex than the underdoped region. The superconductivity in YBCO only exists up to $p \approx 0.25$. The normal state can be instead explained mainly in terms of a Fermi liquid state. The main characteristic temperature in this region is the coherent temperature (T_{coh}), where the electronic excitation starts to become more coherent leading to the restoration of Fermi liquid behaviour. However, recent studies have shown that unconventional behaviors exist in cuprates in both normal and superconducting states of overdoped cuprates. Examples are the formation of cooper pairs at a temperature higher than T_c [86], highly anisotropic Fermi liquid quasiparticle excitation [87], and the emergence of charge order in the overdoped region [88]. The results suggested a departure of the Fermi liquid behaviour, which prompted the research community to investigate more into the overdoped cuprates. The study of overdoped YBCO is currently limited because by adding oxygen the maximum doping one can achieve is $p \sim 0.19$ (e.g., see [89]). Hence, unconventional doping methods are required to achieve a high level of hole doping [90, 91].

2.3 Electronic Nematicity in Cuprates

Nematic phase, also referred to as electronic liquid crystal phase, is the phase where the electronic structure preserves the translational symmetry while spontaneously breaking four-fold (C_4) rotational symmetry [92]. In analogous to the classical liquid crystal [93], the ground state of this phase is somewhere between a 'liquid' (large quantum fluctuations) and a 'solid' (small quantum fluctuations). The idea of the nematic phase in curates was introduced after the discovery of stripe orders, dynamical modulations of charge and spin in the form of 'stripes', in lanthanum-based cuprates and nickel oxides [94]. Besides cuprates, the nematic phase is also observed in other unconventional superconductors, such as iron-based superconductors [95] and heavy-fermion materials [96], and topological superconductors [97].

In iron-based superconductors, the presence of a nematic phase is supported by the direct observation of an anisotropic superconducting gap through techniques such as ARPES, STM, and neutron scattering [98]. For cuprates, the evidence for the presence of a nematic phase is less obvious due to its characteristics, such as short-range orders and small energy scale [99, 100]. Since the nematic phase is also characterized by wavevector Q=0 (translational invariance), the detection using the spectroscopy technique has proven to be difficult as the elastic scattering components dominate [101]. Hence, the presence of nematicity in cuprate has been indirectly observed through, for example, the study of $\rho(T)$ behavior, Nernst coefficient, and magnetic susceptibility [102–104]. In addition, the hint of a nematic phase has been discovered using ARPES. It was found that there are small differences between the $(\pi, 0)$ and $(0, \pi)$ in the Pseudogap region of B2212 revealed by the circular dichroism method. The evidence points towards the possible breaking of rotational symmetry, a main characteristic of nematicity.

There is evidence suggesting that strain could play an important role in the formation of the nematic phase. S. Nakata, et al. [92] reported some differences between the $(-\pi, 0)$ and $(0, \pi)$ points of the Fermi surface when the uniaxial strain was applied to Pb-Bi2212. The anisotropy in the data is only visible in the pseudogap region, and the anisotropy is related to the breaking of C_4 symmetry. In addition, our group reported an unusual anisotropy in the $\rho(T)$ measurement of underdoped ultrathin (10 nm) YBCO

films grown on MgO (110) substrates [20]. When compared to the 50 nm thick films, which behave similarly to bulk materials (**Figure 2.7(a)**), the $\rho(T)$ shows additional anisotropy (**Figure 2.7(b)**) along the two in-plane crystallographic directions that cannot be simply explained by the structural contributions (e.g., from the CuO chains). The anisotropy can be interpreted using the following Boltzmann transport model for electrical conductivity

$$\sigma_{a,b}(T) = 2e^2 \sum_k \frac{v_{F_{a,b}}^2}{\Gamma(k)} \{-n'_F\} \tag{2.8}$$

where v_F is the Fermi velocity, $\Gamma(k)$ is the k-dependent scattering rate, and n'_F is the derivative of Fermi distribution. The key parameter is the ratio $\Gamma(k)/v_{F_{a,b}}^2$ which is directly proportional to the slope of $\rho(T)$. Since the $\Gamma(k)$ is related to the local density of states, $\Gamma(k)$ is proportional to $1/v_F$. Hence, the slope of $\rho(T)$ is proportional only to v_F. The anisotropy in $\rho(T)$ is then related to the anisotropic Fermi velocity where $v_{F,b} \gg v_{F,a}$, meaning that the Fermi surface becomes highly anisotropic as depicted in **Figure 2.7(c)**), where the electronic states are suppressed along the b-axis of the YBCO crystallographic directions. The presence of such a Fermi surface would break the C_4 rotational symmetry, which signals the presence of a nematic phase in the ultrathin YBCO films. If this scenario is true, the anisotropic Fermi surface will result in anisotropic e-ph coupling between the two in-plane crystallographic directions (a and b). One of the ways to confirm the presence of the nematic phase is to investigate the heat transport properties along the in-plane directions, which is the method used in this thesis.

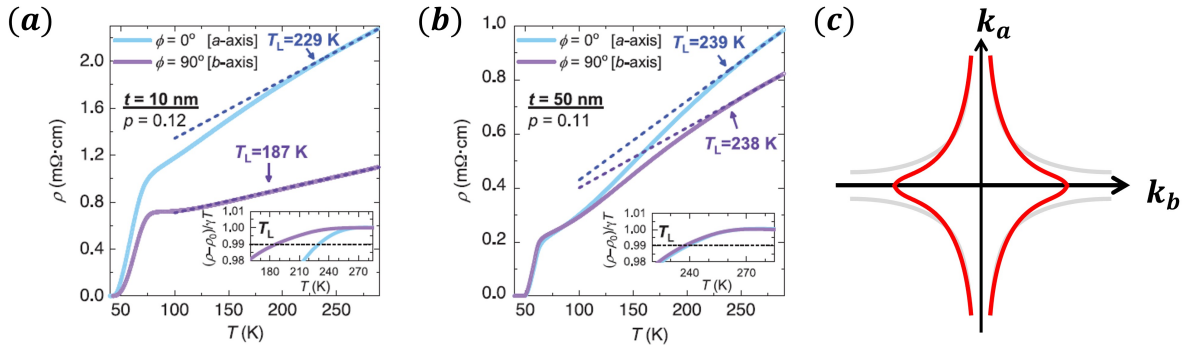

Figure 2.7: The $\rho(T)$ of (a) 50 nm and (b) 10 nm thick, underdoped YBCO nanowires aligning on the different in-plane crystallographic axes. (c) illustrates the anisotropic Fermi Surface as interpreted from the $\rho(T)$ (b), which hints at the presence of a nematic phase [20]

3

Deposition and Characterization of YBCO thin films

The first and most important step in this thesis is the deposition of YBCO thin films. The important benefit of studying cuprate HTS with thin films is that we can have precise control over the composition and morphology. This allows for a systematic study of the materials' properties. The deposition is usually under high temperatures, resulting in the reduction of defect density (thus higher purity). Furthermore, thin films serve as a foundation for fabricating devices. Examples are superconducting quantum interference devices (SQUIDs) [105, 106], which are very sensitive magnetic field detectors, and single-photon detectors [107, 108]. For this thesis, the nanowire structure is used to investigate the anisotropic properties of strained YBCO.

This chapter describes the thin film deposition of YBCO, including ultrathin films, along with important characterization techniques for analyzing their morphology, structural, and transport properties.

3.1 Thin Film Fabrication – Pulsed Laser Deposition

Many aspects must be considered for the growth of YBCO thin films. Aside from having a complex structure, the properties of YBCO (and cuprates in general) are highly dependent on stoichiometry, especially the amount of oxygen doping because the properties are highly dependent on the doping level. Thus, precise control over the stoichiometry in the thin film is the key to preserving the pristine properties of YBCO. The preferred method to deposit high-quality YBCO thin films is epitaxial growth which can be done by a variety of techniques. Some examples include pulsed laser deposition (PLD), molecular beam epitaxy (MBE), and dc/rf magnetron sputtering.

In this thesis work, PLD is used to deposit YBCO thin films. The illustration of the PLD system is shown in **Figure 3.1**. The PLD technique holds several advantages for thin film deposition. The important advantages are the ability to preserve the correct stoichiometry of the deposited materials, and the flexibility to modify deposition conditions to tailor the properties of YBCO. However, the control over the deposition conditions is complex because many deposition parameters have to be optimized.

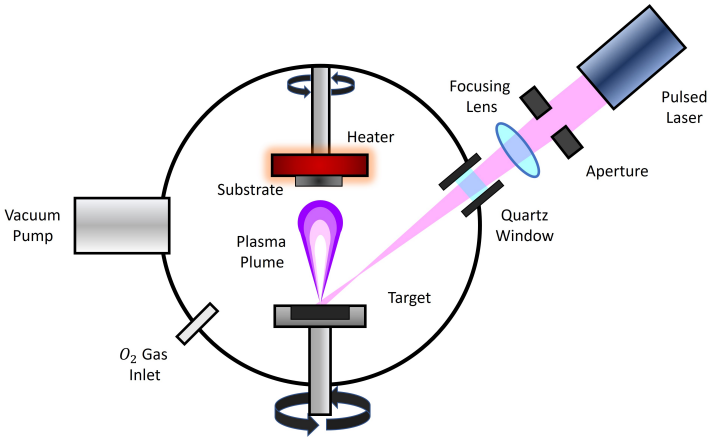

Figure 3.1: Illustration of the PLD system used to deposit YBCO thin films (adapted from [34]).

The main principle of the PLD is the laser ablation of the target material. When a pulse of laser is focused on the target material, the surface of the target (e.g., bulk YBCO) is vaporized and ionized to form a plasma that is ejected from the target's surface as a plume. The ejected materials adsorb onto the surface of the heated substrate. The stoichiometry of the ablaze materials depends on the dynamic of the plasma plume, which is affected by the laser fluence (E), pulse repetition rate (f), and background oxygen partial pressure (P_d). The substrate temperature (T_d) and target-substrate distance (d) also determine the adsorption and diffusion of the adatoms, affecting the nucleation and growth of YBCO thin film. The thickness of the film is determined by the number of laser pulses (n). Right after the deposition, the oxygen is depleted from the structure due to high substrate temperature. This results in the parent compound, $YBa_2Cu_3O_6$, with a tetragonal structure. Oxygen is reintroduced into the structure during the post-annealing process in which the level of doping is determined by post-annealing oxygen pressure (P_{ann}). Since this thesis focuses on the YBCO **near the optimally doped region ($p \sim 0.16$)**, the P_{ann} is set close to the atmospheric pressure.

T_d (°C)	P_d(mbar)	E(mJ)	f(Hz)	d(mm)	P_{ann} (Torr)
760	0.6	55	6	55	650

Table 3.1: Deposition condition for optimally doped YBCO thin film.

3.2 Substrate, Strain, and Twinning of YBCO Film

The selection of the substrate is of great importance for the epitaxial growth process, as it determines the crystallographic structure and orientation of the growth materials. To fabricate the YBCO thin films with properties similar to the bulk counterpart, one must consider not only the crystal structure of the substrate but also the in-plane lattice parameters of the substrate as well. The reason is that the lattice mismatch can induce stress to the thin film, resulting in a strained YBCO structure. The lattice mismatch, quantifying the strain, is defined as

$$\delta^m = \frac{a_s - a_{film}}{a_s} \tag{3.1}$$

where a_s and a_{film} are lattice parameters of the substrate and thin film, respectively. The amount of lattice mismatch needs to be considered carefully because the strain accumulation will result in irreversible deformation and defects through, for example, strain relaxation. Hence, the typical lattice mismatch for the epitaxial growth of high-quality thin film is less than 1%. However, the acceptable lattice mismatch for depositing YBCO thin film can be higher, since the film thickness selected for this thesis ranges from very to ultra-thin (e.g., only 50-10 nm).

The preferred choice of substrates for growing YBCO thin film is oxide materials, such as $SrTiO_3$ (STO), $LaAlO_3$ (LAO), LSAT, and MgO. These oxide materials have similar lattice parameters and thermal properties to YBCO. For example, the δ^m between YBCO and STO(001) is typically 2%, while the value for YBCO/MgO(001) is 9% [109]. **Table 3.2** summarizes lattice parameters of these well-known substrates and optimally doped YBCO. It is noted that the lattice mismatch also depends on the crystallographic orientation of the substrate's surface. In addition, these oxide materials are chemically stable and compatible with cuprates.

Material & Orientation	In-Plane Lattice Parameters (Å)
YBCO (Optimally Doped)	$a = 3.82; b = 3.89$
STO(001)	$a = b = 3.91$
LAO(001)	$a \approx b = 3.79$
MgO(001)	$a = b = 4.21$
MgO(110)	$a = 4.21; b = 5.96$

Table 3.2: YBCO and substrate in-plane lattice parameters. The data is taken from [105] and https://www.mtixtl.com/laalo3.aspx.

When oxygen is introduced into the structure, it is expected that the YBCO should exhibit some anisotropy in the transport properties due to the contributions from CuO chains. However, the growth of YBCO can lead to the formation of multiple regions that have different crystal orientations related to certain symmetry operations, ultimately causing a loss of anisotropy. This phenomenon is known as twinning [110]. There are two types of twin pairs in YBCO: one that aligns along [110] diagonal plane and another that aligns along $[\bar{1}\bar{1}0]$ diagonal plane with respect to the tetragonal structure. The twinning happens when YBCO is deposited on the substrate with a square in-plane lattice, in which the YBCO films experience random exchange between the *a*- and *b*-axis. This causes the loss of orthorhombicity in the thin film structure because the unidirectional CuO chain does not have a preferred crystallographic alignment (e.g., they align along both a and b directions).

To enhance anisotropy, both twinning states must be suppressed during the deposition. A possible way to achieve this is to apply anisotropic strain by selecting the right substrate. The substrate needs to have an asymmetric in-plane structure, so a substrate with a cubic or tetragonal structure (e.g., STO(001) and LAO(001)) cannot be used to obtain the untwinned films. Then, it is necessary to perform surface treatments on these substrates to introduce additional anisotropy, such as STO(001) substrates with a vicinal angle [109]. Another way to introduce anisotropic strain is to use substrates with anisotropic in-plane lattice, which is the main method used in this thesis.

3.3 YBCO Thin Film on MgO(110) – Towards Untwinned Films

Since this work focuses on the anisotropic properties of YBCO thin film, the films were mainly grown on [110]−oriented MgO, or MgO(110), substrate. MgO(110) has a rock-salt crystal structure with anisotropic in-plane lattice parameters of [100] = 4.21 Å and $[1\bar{1}0] = 5.96$ Å, which induces lattice mismatch of 8% and 35% respectively to the thin film. MgO also has the thermal expansion coefficient of $10.5 \times 10^{-6}/K$, which is similar to YBCO [111]. The thermal expansion coefficient is very important for the high-temperature deposition since the typical T_d lies between $700-900°C$ for YBCO deposition in the PLD system. However, MgO(110) by itself cannot be used to suppress the twinning states of YBCO. It was discovered that the MgO(110) substrate induces peculiarly small strain to the thin film despite a large lattice mismatch. Therefore, additional anisotropy has to be introduced to obtain untwinned films.

3.3.1 Untwinned YBCO films on MgO(110)

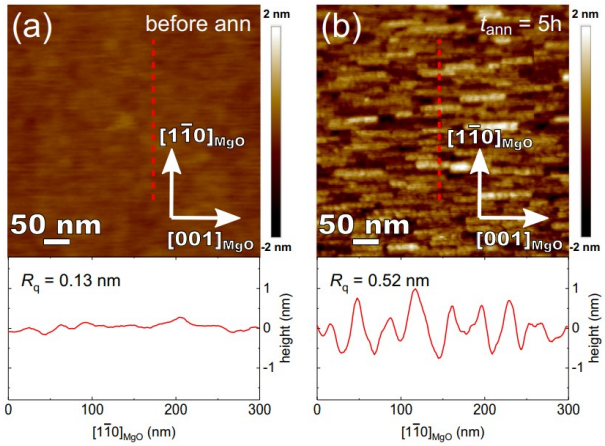

Figure 3.2: AFM images of MgO(110) surface [108]. (a) shows a surface before annealing, while (b) shows a surface reconstruction after 5 hours of annealing at $T = 770°C$ resulting in the formation of micro/nano facets.

The surface treatment to introduce additional anisotropy can be done by thermally annealing a MgO(110) substrate at $T = 770°C$ and $P = P_d$ before YBCO deposition. The annealing process causes the surface reconstruction of MgO(110) into micro/nanofacets that orient along [001] MgO directions (or the b-axis of the YBCO crystal structure). The comparison between unannealed and annealed surfaces is shown in **Figure 3.2**. These structures induce additional anisotropic strain that can suppress the formation of twinning planes [109]. According to the previous reports, the surface reconstruction is fully formed after two hours of annealing and the effect of annealing starts to saturate after five hours. Hence, the annealing time of $t_{ann} = 5$ hours is chosen to optimize the trade-off between the processing efficiency and the untwinning rate. In addition to the annealing process, the thermodynamics of the YBCO growth also plays an important role in the formation of twin planes. Hence, the deposition parameters were optimized to maximize the untwinning rate (see **Table 3.1** for the values).

The tool used to analyze the structural properties of YBCO thin film is X-ray diffraction (XRD). Symmetric $2\theta - \omega$ was performed to investigate the crystallinity and the orientation of the film. An example of the data is shown in **Figure 3.3**. From the figure, the scanning clearly shows the (00n) Bragg reflection that indicates the *c*-axis oriented growth. From the angular position of these peaks, the *c*-axis parameter can be derived by using Bragg's law: $n\lambda = 2d\sin\theta$, where λ is the wavelength of x-ray and n is the position of Bragg's peak. The estimated *c*-axis length is shown in the figure. The value of the *c*-axis parameter can provide some information about the strain by comparing it to the bulk value. Typically, the value of the *c*-axis length decreases with increasing oxygen doping. The formation of the CuO chain stretches the *b*-axis while the *a*-axis remains the same, so the *c*-axis shrinks to preserve the volume of the unit cell. However, the information has to be interpreted along with the T_c value to accurately estimate the doping level.

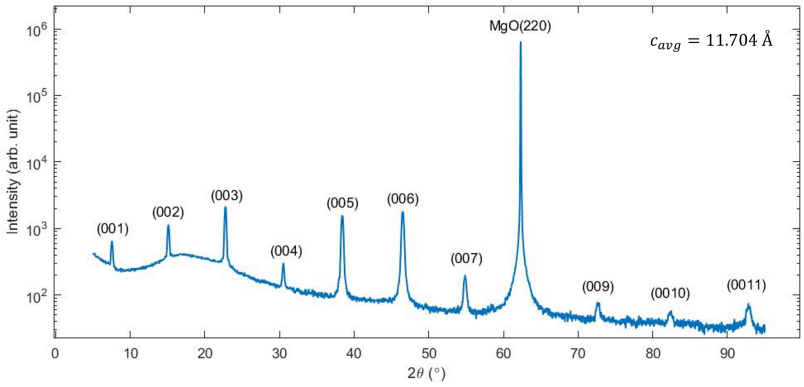

Figure 3.3: Symmetric $2\theta - \omega$ scanning of YBCO film on MgO(110). The c-axis parameter can be extracted from the peak position using Bragg's law.

The rocking curve, which is the $\Delta\omega$ scan associated with the (00n) peak, provides information about the level of mosaicity or "degree of perfection" of the crystal. An example of a rocking curve scan from (006) is shown in **Figure 3.4**. In principle, the width of the rocking curve depends on the mosaicity. The better the crystal grains align, the narrower and more intense the peak becomes. The peak shown in Figure is narrow ($FWHM \sim 1°$), indicating the good crystallinity of the films.

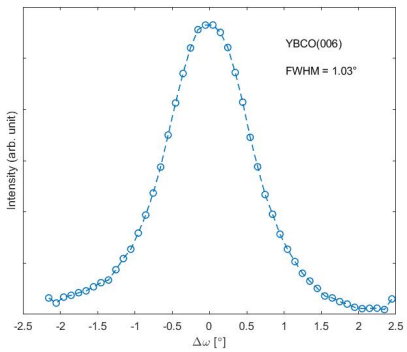

Figure 3.4: Rocking curve of (006) YBCO reflection. The FWHM is about 1°, which determines the high degree of mosaicity in the thin film.

The untwinning degree is also characterized using XRD by performing asymmetric $2\theta - \omega$ scanning around in-plane YBCO (308) and (038) directions, representing a- and b-axis respectively. An example of highly untwinned YBCO films is shown in **Figure 3.5(a)**. The two peaks seen in the maps from each figure represent the contribution from the (308) and (038) directions. From the summation of the asymmetric $2\theta - \omega$ intensity (**Figure 3.5(b)**) the peak with higher intensity lies in the (308) direction. The untwinning rate is estimated by comparing the intensity of a higher peak to the total intensity of both peaks. The shorter peak is suppressed when the untwinning rate increases. With the optimized condition, the untwinning rate of 82% can be achieved as shown in the figure. The lattice parameter of the a- and b-axis can be estimated from the peak positions along (308) and (038), respectively. For this example, $a \sim 3.82$ Å, $b = 3.87$ Å. Compared to the bulk values [111], the b-axis length shrinks, and the c-axis length expands while the a-axis length remains almost the same. This means that the strain is compressive along the b-axis when depositing YBCO on MgO(110). The effects of the unidirectional strain will be further emphasized when discussing ultrathin films.

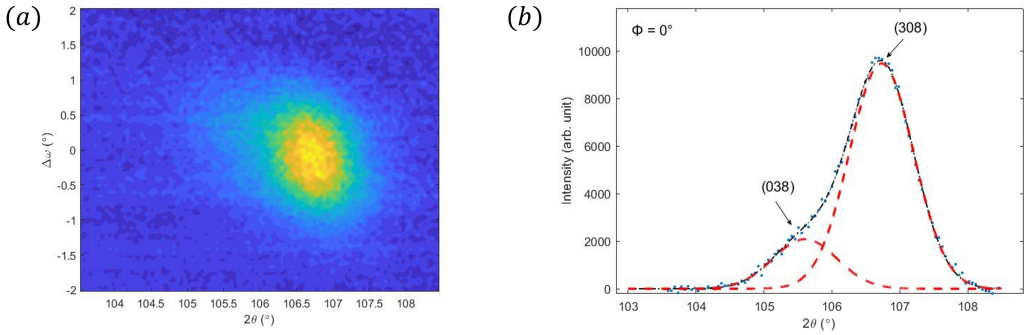

Figure 3.5: (a) The asymmetric $2\theta - \omega$ mapping around YBCO (308)/(038) Bragg reflections of a highly untwinned YBCO. (b) shows the summation of the asymmetric $2\theta - \omega$ intensity where two Gaussian curves are fitted to analyze the individual contributions from (308) and (038).

3.3.2 Transport Characterization

The transport properties are also investigated to observe the anisotropy in the YBCO thin film. This is done by measuring resistance vs. temperature $R(T)$ along the a- and b-axis using the Van der Pauw method. The example of the $R(T)$ at $p \sim 0.16$ is shown in **Figure 3.6**. The T-linear trend is the key indicator of the strange metallicity. Without taking the twinning effect into account, the transport is expected to be anisotropic along the in-plane directions due to the contribution from CuO chains. For the $R(T)$ measurements, the resistance is expected to be lower along the direction of the chains. The twinning in YBCO films causes the transport to become more isotropic because the random exchange between the a- and b-axis causes the chains to orient along both directions. Then, the films with a high untwinning rate will have higher anisotropy in the transport properties. This is reflected in the anisotropy in $R(T)$ measurement, as shown in **Figure 3.6(a)**. In this case, the resistance is lower along the b-axis meaning that the chains mostly orient along this direction. Another noticeable feature is the anisotropy in the trend of resistance. When looking only at the a-axis, the linearity extends almost down to the T_c. On the other hand, the linearity only extended to some intermediate

temperature (about 200K in this example) for the b-axis, and the $R(T)$ instead shows T^2 dependence due to the contribution from CuO chains.

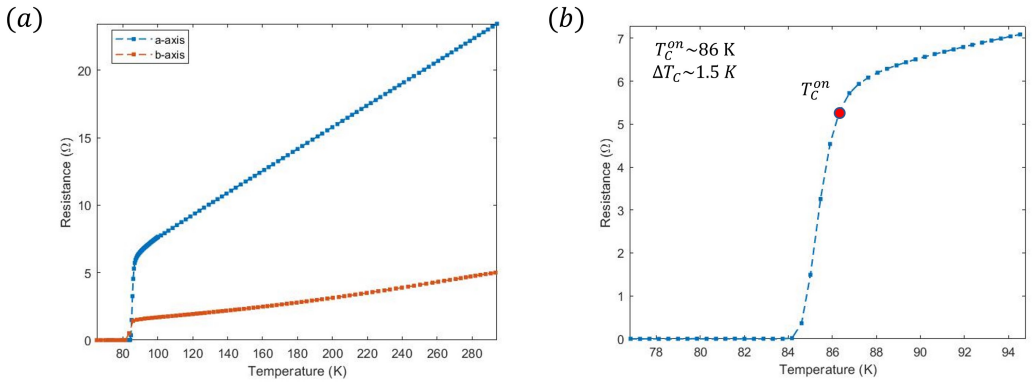

Figure 3.6: (a) An example of the $R(T)$ measurement along a- and b-direction of highly untwinned YBCO films on MgO(110). (b) shows the superconducting transition from the measurement along the a-axis. *The electrical contacts were not in a square here, which explains why the anisotropy factor is so high.

The doping level and uniformity are analyzed from the superconducting transition. The superconducting transition is quantified based on two parameters, the onset temperature (T_c^{on}) and the broadening of T_c (ΔT_c). T_c^{on} is defined at the 90% of the resistance where the transition starts, while ΔT_c is defined based on the FWHM of the dR/dT. The doping uniformity can be estimated by observing the breadth of the superconducting transition. In principle, the sharper the transition, the higher the uniformity. In our case (**Figure 3.6(b)**), it is shown that the ΔT_c is only about 1.5 K, which is close to the transition of a single crystal YBCO [112]. Besides the broadening of the transition, the non-uniformity in the doping profile can be signaled by the presence of multiple transitions. The transition temperature, together with information about the c-axis length from the XRD measurements, can be used to estimate the doping level by applying the following parabolic relationship

$$1 - \frac{T_c}{T_c^{max}} = 82.6 \cdot (p - 0.16)^2 \tag{3.2}$$

where T_c^{max} is the critical temperature at the optimal doping (p=0.16). Since the doping profile is not completely uniform, the best practice would be to use the average T_c instead, which is defined as the maxima of the first derivative of the superconducting transition. The value of the c-axis length determines whether the sample is underdoped or overdoped. For instance, if the c-axis length is smaller than the optimally doped value, it means that the doping is on the overdoped side. The opposite is true for the underdoped samples. Another method to analyze whether the sample is on the underdoped or overdoped side, especially for the near optimally doped region, is to observe the shape of the $R(T)$. For the slightly overdoped samples (**Figure 3.7(a)**), the linear $R(T)$ ends above the transition temperature which marks the end of the strange metal regime. Below such temperature, the typical Fermi liquid nature is recovered causing the $R(T)$ to bend upward just before the transition temperature [82]. For slightly underdoped samples, however, the $R(T)$ bends downwards instead as shown in **Figure 3.7(b)**. The origin of this downward turn is still under debate, but it might be possible that the

phenomenon is due to the contribution from pseudogap and other intertwined orders, including CDW and superconducting order (paraconductivity).

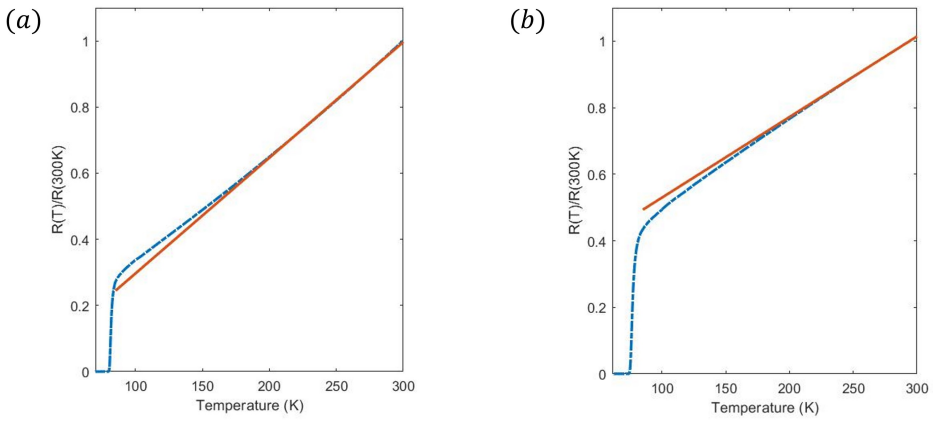

Figure 3.7: Examples of the a-axis $R(T)$ for (a) slightly overdoped and (b) slightly underdoped YBCO thin films. It is noted that the data were taken using the YBCO grown on STO (001), but the behaviour is also similar to the YBCO grown on MgO (110).

3.3.3 Ultrathin YBCO Films

There are interesting consequences when shrinking the thin films down to 10 nm (about 8 to 9 unit cells). Due to such a thin volume of YBCO, the effect of strain induced by the substrate becomes significant. Interestingly for the YBCO thin films grown on MgO (110), the strain becomes tensile rather than compressive. This was evidenced by the expansion of the b-axis and compression of the c-axis length as shown in **Figure 3.8(a)**. The transport properties are also affected. Due to the very small thickness, the doping mechanism during the post-annealing process becomes different from the 50 nm thick films. **Figure 3.8(b)** shows the $R(T)$ near the transition temperature of t=50 nm and t=10 nm films that were deposited under the same growth conditions. The reduction of the T_c^{on} and the increase in ΔT_c are two noticeable changes in the transition behaviour when compared to thick films. Based on the shape of $R(T)$ of the a-axis (**Figure 3.8(c)**), the reduction of T_c^{on} indicates that the thin film is more overdoped which is possibly due to the better oxygenation of the thinner film during the annealing process. The increase in ΔT_c in the optimally doped region is attributed to the additional disorder caused by, for example, inhomogeneous doping of the films. In addition, the untwinning rate in ultrathin films is enhanced, even reaching above 90% (e.g., see **Figure 3.9**), which means that the effect of anisotropy is also enhanced in the ultrathin films.

A striking feature of the ultrathin YBCO films deposited on the MgO substrate is the additional anisotropy of the resistivity along the a- and b-axis that is hypothesized to be a consequence of an anisotropic Fermi surface, as discussed in the previous chapter. It was also discovered that this anisotropic behaviour persists up to the optimally doped region of the phase diagram.

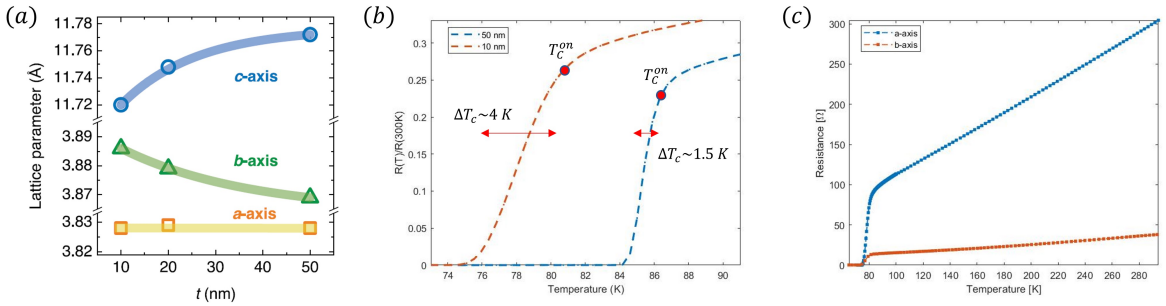

Figure 3.8: (a) Lattice parameters of YBCO thin film at different thicknesses (the data is taken from [20]). Panel (b) shows the comparison of $R(T)$ superconducting transition between t=50 nm and t=10 nm films, while panel (c) compares a- and b- axis of t=10 nm film. It is noted that four-point contacts were not a perfect square, so the anisotropy is also exaggerated.

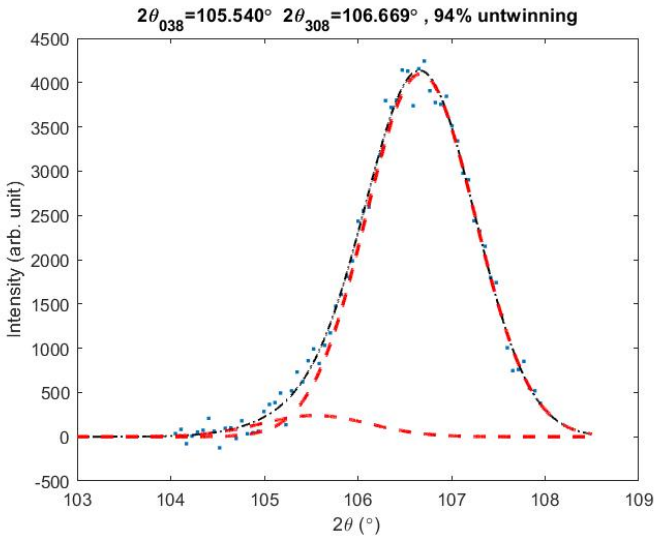

Figure 3.9: Integration over *omega* of the asymmetric $2\theta - \omega$ mapping around YBCO (308)/(038) Bragg reflections of an ultrathin YBCO film deposited on annealed MgO. The untwinning rate of this film is 94%.

4

Fabrication of YBCO Nanowires

For this thesis work, nanowires are used to investigate the in-plane heat transport properties of YBCO thin films. Aside from the ability to tune the dimensions, nanowires are used to highlight the in-plane anisotropy in the YBCO by comparing the transport properties of the wires aligned along different crystallographic directions. The most challenging aspect of patterning YBCO nanowires is to preserve the pristine bulk properties during the fabrication process, as the YBCO is very sensitive to the environment and defects due to chemical instability (easy oxygen out-diffusion) and it is characterized by a very short coherent length ξ. This chapter provides an overview of the fabrication process of YBCO nanowires that still preserve the pristine HTS properties.

4.1 Nanofabrication process of YBCO nanowires

The nanofabrication process used to pattern YBCO nanowires has been optimized by our group over a decade [113–115] and it revealed to be successful for different HTS compounds [116]. Here, we use electron-beam lithography in combination with an amorphous carbon hard mask and a gentle ion milling process. The carbon mask was chosen because of its durability when subjected to ion milling and the capacity to be removed using oxygen plasma. In addition to the ability to preserve the superconducting properties of YBCO thin films [89], it was shown that the nanowires exhibit a high critical current that is close to the theoretical depairing limit which is a point where the cooper pair breaks [113, 117]. The following is the overview of the nanofabrication (see **Figure 4.1** for the illustration):

1. A 35 nm thick gold pattern is deposited ex-situ on top of the YBCO thin film by sputtering. The gold pattern functions as a connecting surface for the wire bonding process during the transport measurement.
2. A layer of amorphous carbon, acting as a protective layer for YBCO, is deposited by PLD on top soon after the gold sputtering process. The carbon deposition is done in three steps with increasing energy to ensure better adhesion of carbon onto the surface. Then, two positive resist layers corresponding to two sensitivities to the electron beam are spin-coated on top of the carbon film.
3. The nanowire geometry is defined by electron beam lithography using a 100 kV beam. The exposed area is removed during the resist development.
4. A layer of chromium, acting as a mask for carbon, is deposited on top using an electron beam evaporator.
5. A part of chromium is removed from the sample through a lift-off process, which defines the mask pattern for the ion milling process in the later step.

6. A part of carbon film that is not covered by chromium is removed by low-power oxygen plasma etching. It is important to use low-power etching because the oxygen plasma can introduce oxygen vacancies to the YBCO under the carbon.

7. The chromium layer and YBCO not covered by carbon are etched by Ar^+ ion-beam milling. The etching parameters (e.g., accelerating voltage, beam current, and time) were optimized to the lowest threshold to minimize the damage to the pattern structures. The heat generated from the impact of the ions can be detrimental to the YBCO structure, as YBCO is already chemically unstable making it prone to oxygen out-diffusion at high temperatures. Hence, a cooled stage is used to minimize the heating effect during the whole process.

8. The rest of the carbon layer is removed through another round of oxygen plasma etching.

Examples of the optical and SEM images of the final device are shown in **Figure 4.2**. It is noted that the parameters for ion milling and plasma etching have been chosen differently for the 50 nm and 10 nm films. This is because the 10 nm films are even more susceptible to the environment and defects than the 50 nm films. We can further preserve the properties of nanowires by introducing a gold capping throughout the whole surface [114], but it would not be possible to study the normal state of YBCO nanowires as the whole wire is shorted.

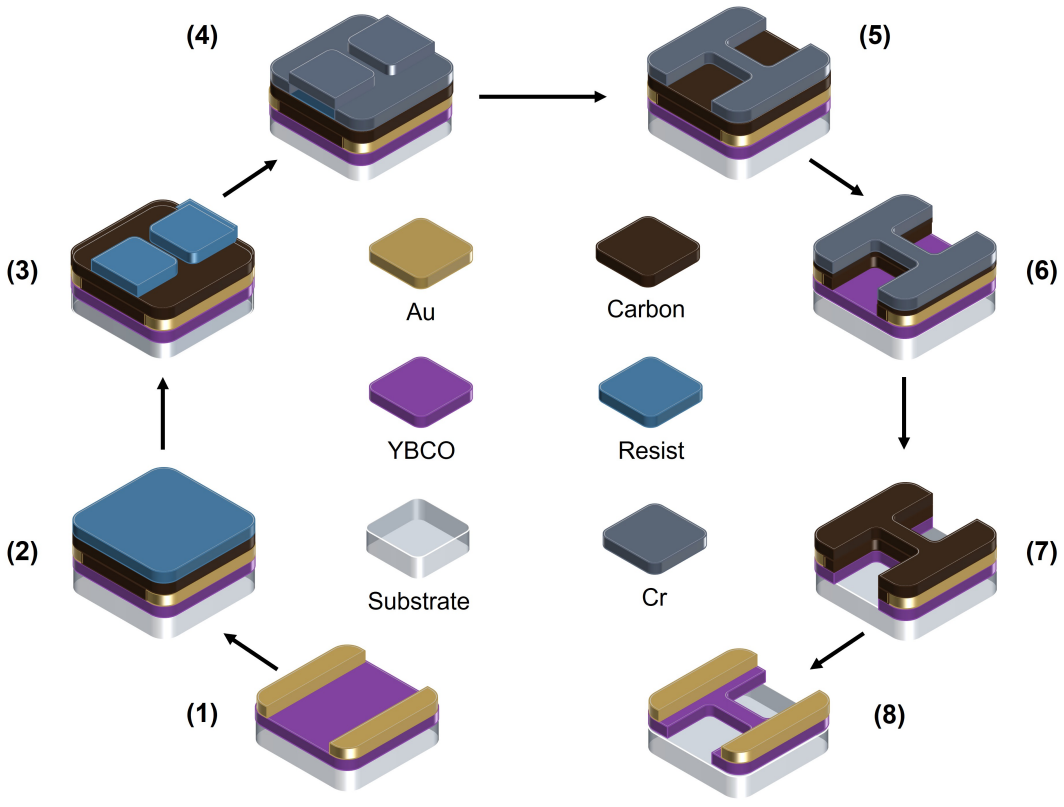

Figure 4.1: Overall nanofabrication process of YBCO nanowires from a thin film.

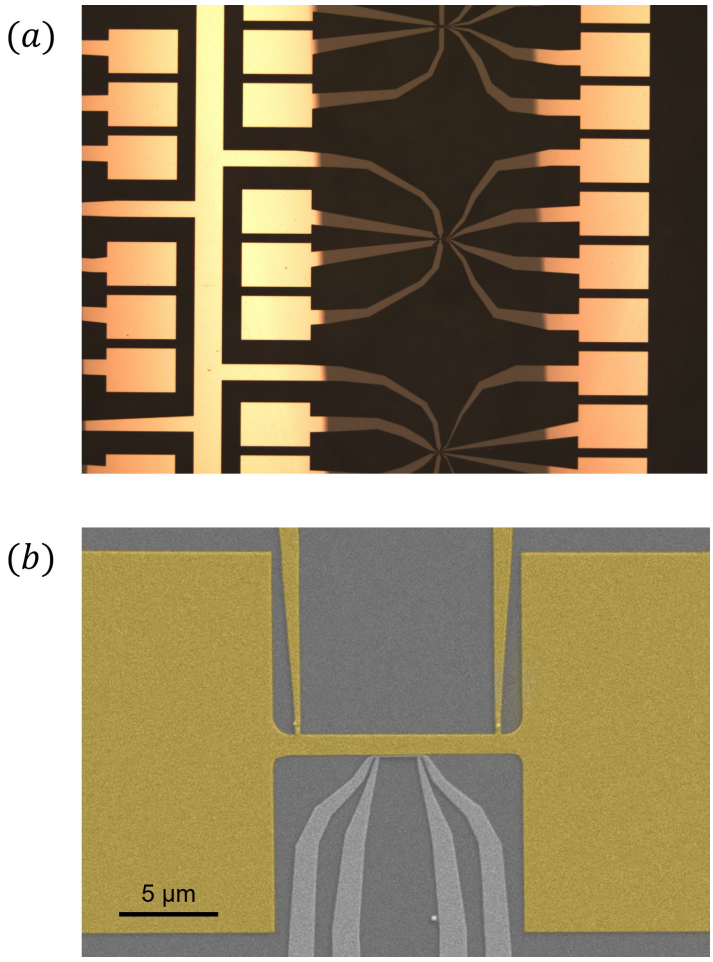

Figure 4.2: The (a) optical and (b) false color SEM image of the YBCO nanowires. The bright part in (a) indicates the gold contact region. It is noted that the small nanowires located very close to the bridge were initially designed to act as local thermometers. However, the experiment setup has not been modified to use those thermometers yet.

5

Transport in YBCO nanowires

In this thesis work, nanowires are used to study the anisotropic Fermi surface in YBCO by extracting information related to the electrical and heat transport properties of the nanowires oriented along different crystallographic directions. This chapter aims to provide an overview of the electrical and heat transport properties of the YBCO nanowires and discuss the design to probe the heating effects.

5.1 Transport properties of YBCO Nanowires

When the electrical power is injected into a conducting nanowire (or conducting wires in general), the wire heats up due to the Joule heating effect. This phenomenon also happens in the normal states of YBCO nanowires near the optimally doped region because they still behave as conductors even though they display strange properties. The heat generated from the injected power dissipates through multiple systems which can be imagined as a series of thermal resistors. The simple illustration is shown in **Figure 5.1**.

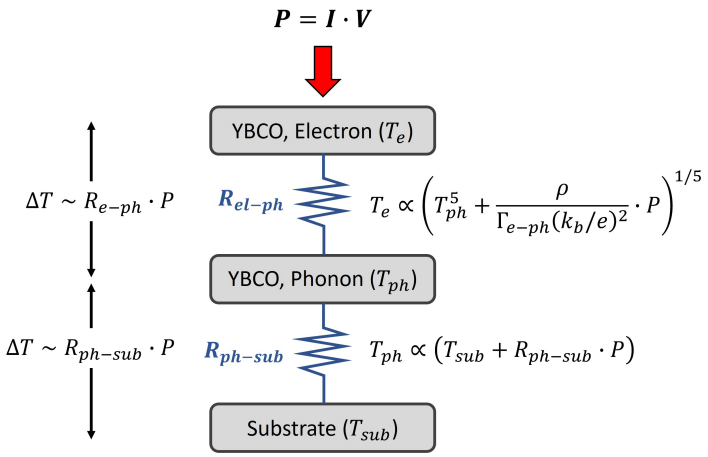

Figure 5.1: Simplified illustration of the heat transfer through a series of thermal resistors in a YBCO nanowire.

The model of the heat transport by applied electrical power is developed based on the YBCO heat transport equations without the effect of e-ph coupling [118] and the e-ph coupling in normal metals at the low-temperature limit [119]. The additional term from e-ph coupling might not be accurate because cuprates are based on strongly correlated electrons. However, there is no report on the heat transport model of the strange metals, at least to our knowledge. The full derivation and explanation for this simplified case will be shown in **Appendix A**. For the long nanowire ($L \gg l_{e-ph}$, l_0 where l_{e-ph} is the e-ph scattering length and l_0 is the thermal relaxation length), the contribution from thermal conductivity (or heat dissipation from nanowire into the electrode) can be ignored as $\frac{\partial T}{\partial x} = 0$. The relationships between electron and phonon temperature (T_e and T_{ph}) and the applied power under the steady state ($\frac{\partial T}{\partial t} = 0$) are

$$T_e \propto (T_{ph}^5 + \frac{\rho}{\Gamma_{e-ph}(k_b/e)^2} P)^{1/5} \tag{5.1}$$

$$T_{ph} \propto (T_{sub} + R_{ph-sub} \cdot P) \tag{5.2}$$

The explanation of the thermal resistor in **Figure 5.1** is as follows. Firstly, the power is converted into heat due to Joule heating. The generated heat is then dissipated firstly into the YBCO electronic system of the YBCO. Due to e-ph coupling, the heat from the electronic system is dissipated into the YBCO phononic system. Lastly, the heat from the YBCO phononic system is dissipated into the substrate through the interface scattering. Hence, the heat dissipation goes through two thermal resistance channels: Electron-phonon scattering (equation 5.1) and interface (Kapitza) conductance (equation 5.2).

To illustrate the validity of the assumptions, the calculation for the steady-state heating profile of the YBCO nanowire is shown in **Figure 5.2(b)** [118]. The calculation was done at high temperatures, where the Kapitza conductance dominates over the contribution from e-ph coupling inside the nanowire, making the e-ph term negligible. The temperature is stable in the middle of the wire, and the effect of thermal relaxation from the nanowire into the electrodes (bath), which has a length scale of approximately $l_0 \sim 200$ nm for the YBCO nanowire with $t = 50$ nm, is quite negligible for the long wire. This heating profile is suitable for the study since the only terms affecting the heating in the stabilized region are the Kapitza conductance and e-ph coupling. If the length is too short, thermal relaxation will dominate the heating profile, making the study of e-ph coupling more complicated due to the contribution of the thermal conductivity term.

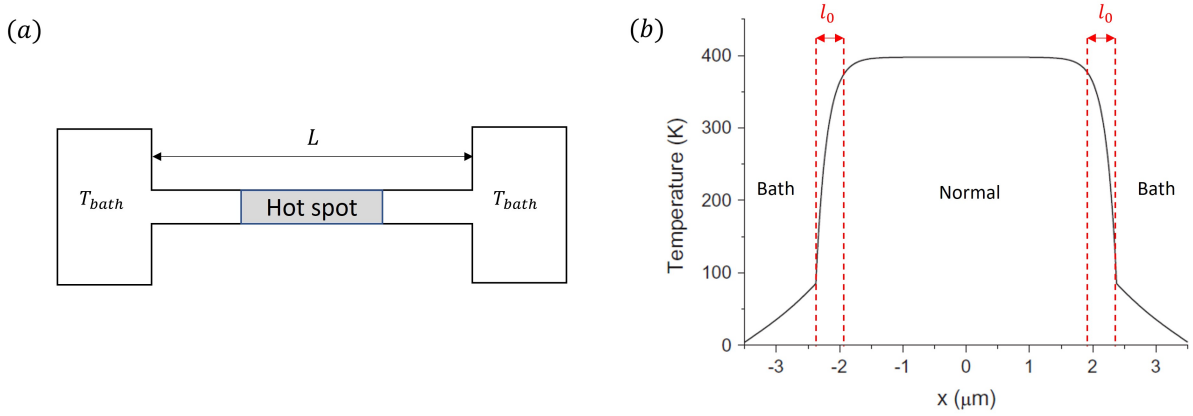

Figure 5.2: (a) The geometry of the YBCO nanowire used for the calculation (b) the simulated heating profile from [113].

The effect of heat conduction through the interface between the nanowire and the substrate is much more pronounced than the effect of e-ph coupling, especially at higher temperatures. Typically for normal metals, the experiments need to be done at very low temperatures (e.g., millikelvins [119]) to directly observe the effect of e-ph coupling. However, the superconducting order in YBCO complicates the measurement at low temperatures. It is possible to suppress the superconductivity by applying a magnetic field, but it would require an extremely high field of 100 Tesla for optimally doped YBCO [17]. Nevertheless, the effect of e-ph coupling can still be indirectly observed, at least theoretically, by analyzing how the temperature evolves with applied electrical power $T(P)$. Based on the relations above, the temperature for the Kapitza term would evolve linearly as $T_{ph} \propto P$, while the phonon temperature would evolve according to the power law with $T_{el} \propto P^{1/5}$. Therefore, it would be possible to observe the effect of e-ph coupling if there is any deviation from the linearity of the total $T(P)$.

Observing just the trend is not sufficient to identify the effect of e-ph coupling if the Kapitza conductance significantly dominates the temperature profile. So, the comprehensive parameter used to quantify the effect of heating is the thermal conductivity (in W/Km^2). The total conductivity already includes the effects of the Kapitza conductance and the heat conduction through e-ph coupling. Consequently, any changes in the total thermal conductivity value from the Kapitza conductivity would serve as indicators for the e-ph coupling contribution. In this analysis, the nanowires are intentionally chosen to be sufficiently long, allowing us to neglect the anisotropic in-plane thermal conductivity between the wire and the electrodes arising from the untwinned YBCO's preferred direction of CuO chains. The heat conduction at the YBCO/MgO interface is found to be similar for nanowires oriented along both the *a*- and *b*-axes. This similarity arises from the isotropic transport along the c-axis. So, the e-ph coupling would be a potential factor causing anisotropy in thermal conductivity. For the thicker YBCO nanowires (e.g., 50 nm), the Fermi surface is isotropic which should result in isotropic thermal conductivity along the in-plane directions. However, in ultrathin nanowires (e.g., 10 nm), anisotropic thermal conductivity is expected due to the anisotropic Fermi surface. In addition, electron-phonon scattering should be enhanced for the thinner structures due to factors such as increased phonon confinement and the surface-to-volume ratio. As a result, the effect of e-ph coupling on the total thermal conductivity should be more pronounced in the ultrathin wires.

5.2 Design and Simulation

Several factors need to be considered when designing the nanowires for our experiments. The dimensions of the nanowires represent the first factor. Since the thickness is fixed from the PLD deposition, only length and width can be controlled during the nanofabrication process. COMSOL simulation was done to visualize the temperature profile according to the selected dimensions. It is noted that the e-ph coupling is dominated by the Kapitza conductance at high temperatures, so the effect of e-ph coupling is neglected in the simulations. Since most of the measurements were done above T_c, the physics of the nanowire is defined based on a normal conductor such as copper. The simulation results for the length and width dependence are shown in **Figure 5.3** and **Figure 5.4**, respectively. For the length dependence, it was discovered that the effect of thermal relaxation is significant when $L = 1$ μm. On the other hand, the profile near the middle of the wire started to become flat, which is similar to **Figure 5.2(b)**, when $L \geq 5$ μm. Therefore, the appropriate lengths are 5 μm or longer. It is noted that shorter wires would be interesting for further investigation of the heating dissipation into the electrodes. The width of the nanowire has to be appropriately chosen to minimize the effect of heat dissipation on both substrate and electrodes. The effect of thermal relaxation is much more significant for wider wires, so it is preferred to choose narrower wires. However, we want to also minimize the effect of the non-uniform width profile of the nanowire, so narrow wires are not desirable. Therefore, the width of the nanowire is selected to be 1 μm for the ease of experiments, and then the length is selected accordingly.

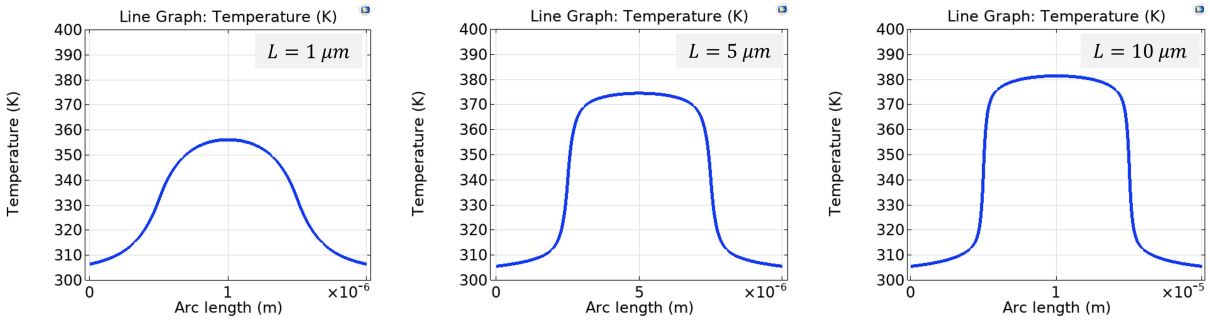

Figure 5.3: COMSOL simulation of the length dependence of the YBCO nanowire. The length and thickness are fixed at 10 μm and 50 nm, respectively.

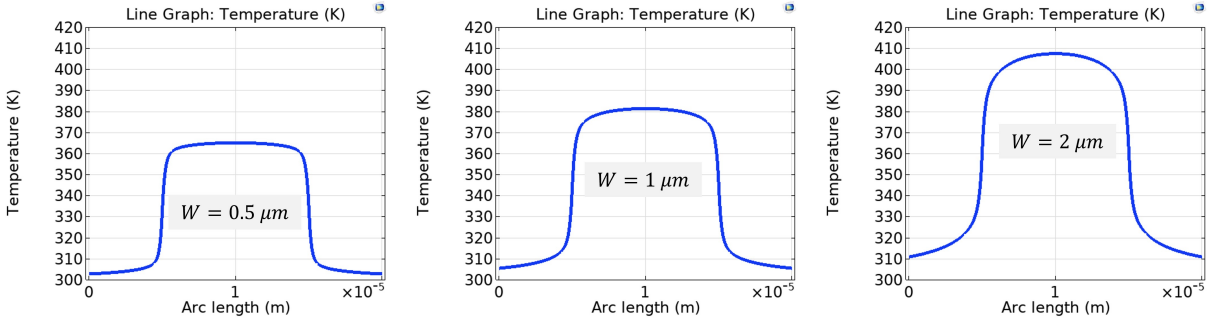

Figure 5.4: COMSOL simulation of the width dependence of the YBCO nanowire. The length and thickness are fixed at 10 μm and 50 nm, respectively. It is shown that the effect of heat dissipation into the electrodes is already severe when increasing the width to 2 μm.

The last factor for the design is the position of the voltage probes. The experiment will be done using the four-point probe configuration to accurately extract the information from the nanowires, as shown in the sketch in **Figure 5.5**. The current is injected across the wire from the terminals, while two probes are attached to/near the nanowires to read the voltage. Since the voltage probes also act as a heat sink (see **Figure 5.6** for the effect), our initial choice was to design the probes to be as narrow as possible (100-200 nm) and the probes were placed near the bath to avoid the effects near the center of the wires (**Figure 5.7(a)**). The first device was fabricated with this design choice, but it was discovered later that this design was not well suited for the experiment because we needed to apply the current density from low (e.g., 2×10^3 A/cm^2) to high (e.g., 4×10^6 A/cm^2). On some occasions, the voltage probes cannot handle such high current density because their width is much narrower than the nanowire. After the first device, we decided to put the voltage probes on the electrode as close to the nanowires as possible (**Figure 5.7(b)**). However, the main trade-off is the accuracy of the heating profile extraction due to thermal relaxation. Still, the wire length is much longer than the thermal relaxation length making it acceptable to neglect this effect.

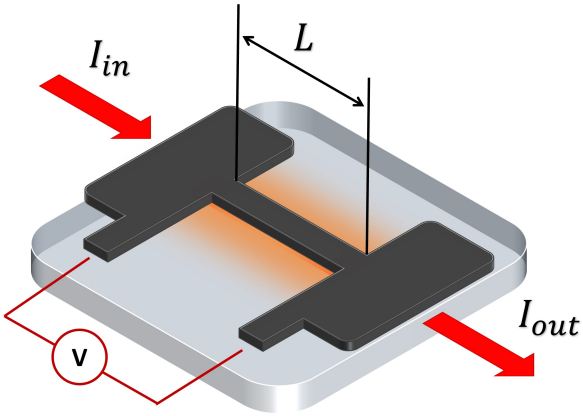

Figure 5.5: Sketch of the nanowire design for the 4-point measurement.

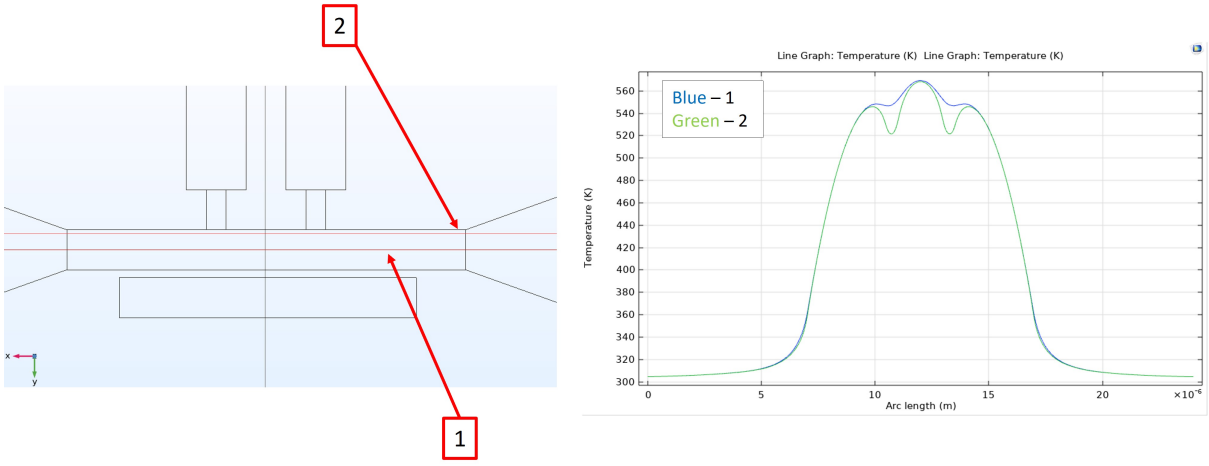

Figure 5.6: Simulation on the effect of the voltage probes on the heating profile of the nanowire. The probe's width is chosen to be 500 nm to highlight the effect of heat dissipation from the wire into the probes.

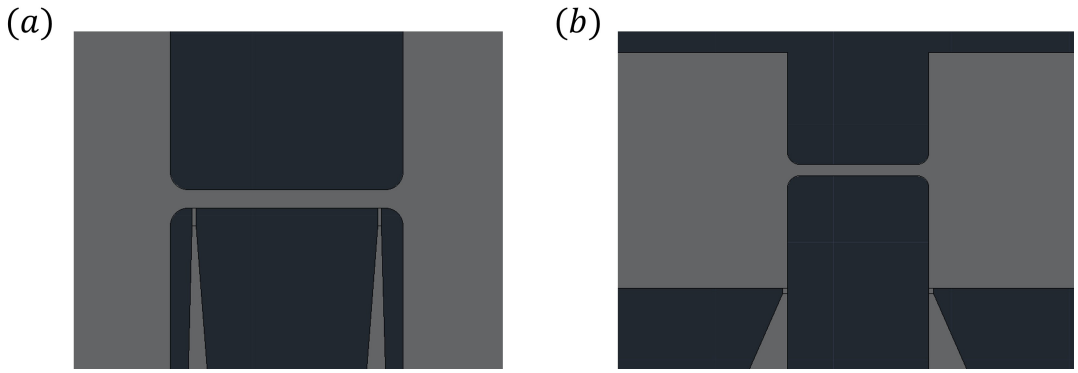

Figure 5.7: The AutoCAD design of the nanowire where the probes are placed (a) on the wire and (b) on the electrodes right next to the wire.

5.3 Measurement Setup to Extracting $T(P)$

The information related to the $T(P)$ can be extracted from the current-voltage (IV) characteristic and the $R(T)$ of the nanowires, as shown in **Figure 5.8**. The IV curve shown in the figure was measured in the superconducting state. When injecting the current in the superconducting state, the current flows in a zero resistive state so the current increases while the voltage remains zero. Above the critical current (I_c), the superconductor undergoes a transition (switching) to a normal state which is indicated by a sudden increase in voltage. For the normal state, the DC resistance (R_{DC}) and injected power can be extracted by using Ohm's law $R_{DC} = V_{DC}/I_{DC}$ and $P = V_{DC} \cdot I_{DC}$. One can track the change in resistance with power using the extracted information. In this example, the slope of the IV curve bends downward at high power, meaning that the resistance increases with power. This effect is an indication of the heating in the nanowires. Then, the temperature can be approximated from extracted R_{DC} to establish the $T(P)$. From $T(P)$, the thermal conductivity can be calculated by using the relation $\kappa = \frac{1}{(\Delta T/\Delta P)} \frac{1}{Area}$ where $\Delta T/\Delta$ P is the slope of $T(P)$. The area was chosen to be the interface area ($A = L \cdot W$) to compare the extracted values with the Kapitza conductance for the YBCO/MgO ($10 - 20 MW/Km^2$ [120]). It is noted that the variation of the Kapitza conductance values is due to multiple factors including the interface quality and the coupling strength between the YBCO and the substrate's atoms.

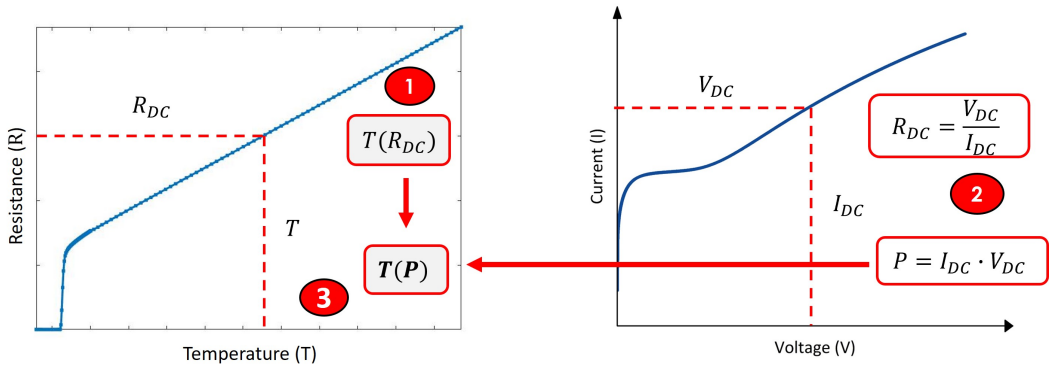

Figure 5.8: The procedure to establish the relationship between the temperature and applied power $T(P)$ from the $R(T)$ and IV characteristics of the nanowires.

The nanowires are measured with a 4 K dip-stick system, which is shown in **Figure 5.9**. The devices are bonded onto the sample holder which is mounted onto the pod located at the end of the dipstick. The whole stick is shielded and filled with helium gas before 'dipping' into the liquid nitrogen to cool down the sample. The helium gas is necessary to prevent moisture from condensing on the devices during the cool-down process. With this setup, the temperature can be stabilized from room temperature down to 82 K.

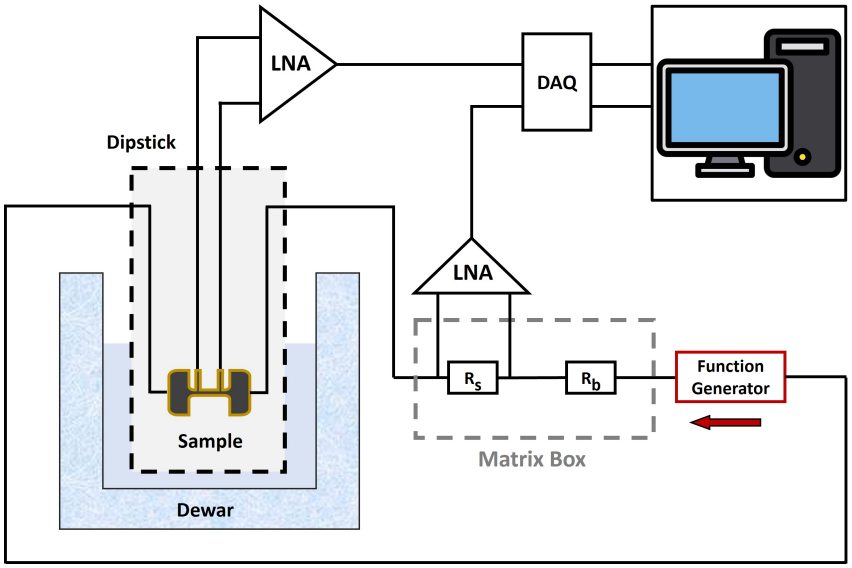

Figure 5.9: Schematics of the 4K dip-stick DC measurement system. It is noted that the only difference between the DC and Lock-In measurement is the addition of LIA after the ADC components.

For this thesis, two types of measurements were employed to measure the IV curve. The corresponding simplified circuits illustrating these measurement setups are shown in **Figure 5.10** and the illustrations of how the IV curve is measured are shown in **Figure 5.11**. The signal from the source denoted as V_s, is controlled by a function generator. The higher ohmic series resistor R_b is used to bias the device, while the lower ohmic resistor R_s acts as a current sensing element that indirectly measures the current. The signals acquired from the current and voltage terminals are then amplified by Low Noise Amplifiers (LNA) and filtered using LC filters before further processing. The first type is the DC measurement which is a typical method to obtain the IV characteristic. For this measurement, a DC bias is applied to the voltage and current terminals and the resulting current and voltage signals are measured and processed by the multimeter. This method directly measures the IV curve. The DC measurement involves applying a triangular voltage bias with a specific frequency that is controlled by a function generator.

The second type is the lock-in measurement, which uses the function generator to send AC signals to the current and voltage terminals. The output voltage signals from the two terminals are demodulated with the Lock-In Amplifiers (LIA). Demodulation is achieved by mixing the AC signals with the synchronized reference signal from the function generator. This mixing process generates multiple frequency components, and unwanted components can be filtered out using low-pass and high-pass filters. The voltage offset is applied to measure the voltage and current at different points, which can be used to reconstruct the IV curve. By employing lock-in amplifiers, the desired signal

can be separated from surrounding noise, resulting in highly accurate measurements, especially at the low-power limit. This makes lock-in measurements preferable to DC measurements in certain scenarios. A comparison between the DC and Lock-In IV-curve will be presented in the next chapter.

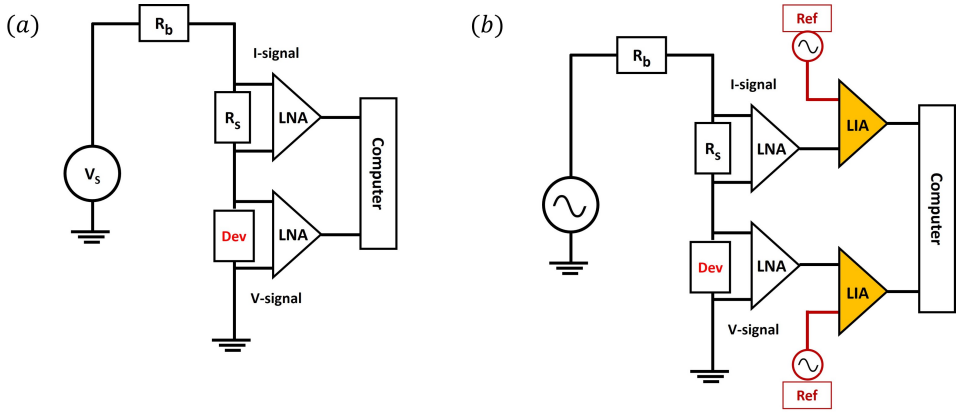

Figure 5.10: The simplified circuits of (a) DC and (b) Lock-In measurements.

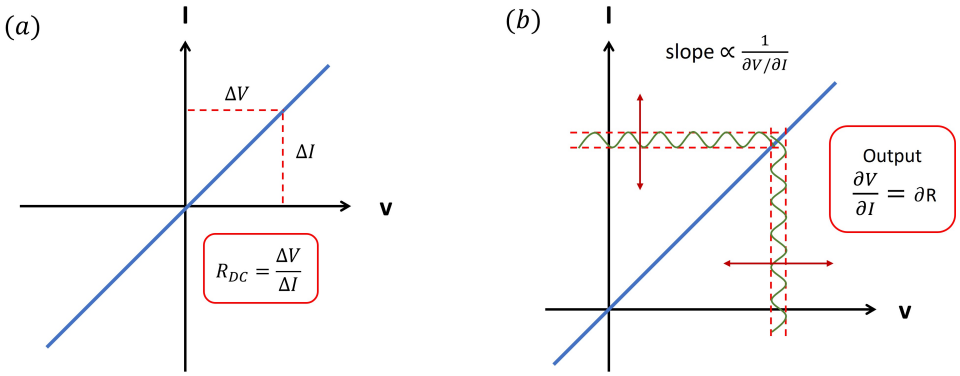

Figure 5.11: The IV curve from (a) DC measurement and (b) lock-in measurements.

To extract the differential current (dI) and differential voltage (dV) from the LIA output signals ($V_{AC}^{voltage}$ and $V_{AC}^{current}$ for voltage and current terminals), the following equations are applied:

$$dV = V_{AC}^{voltage} \cdot \frac{s_V}{r_V} \cdot \frac{1}{G_V} \tag{5.3}$$

$$dI = V_{AC}^{voltage} \cdot \frac{s_I}{r_I} \cdot \frac{1}{G_I} \cdot \frac{1}{R_s} \tag{5.4}$$

where s, r and represents the sensitivity and voltage range of the Lock-In Amplifiers, and G is the gain for the Low Noise Amplifiers. Then, the differential resistance can be simply calculated using $dR = dV/dI$. To reconstruct the complete IV curve, the offset of the DC voltage (V_s) is swept to acquire data points analogous to the DC measurement process (**Figure 5.12**). Each point (n) of the DC voltage can be calculated from the dR and the DC current (I_{DC}), reconstructed by integrating the dI signal, by using the relation $V_{DC} = \int \Delta I_{DC}\, dR$. Since the current measurement setup does not directly measure I_{DC},

the I_{DC} is calculated by calculating the cumulative sum of the dI at each step of V_s by using the following relation

$$I_{DC} = \sum_{i=2}^{n} dI^{i-1} \left(V_S^i - V_s^{i-1} \right) \tag{5.5}$$

where n is the total number of steps. This cumulative sum provides a good estimate of the I_{DC}. However, one should double-check with the values from the DC measurement to get the correction factor.

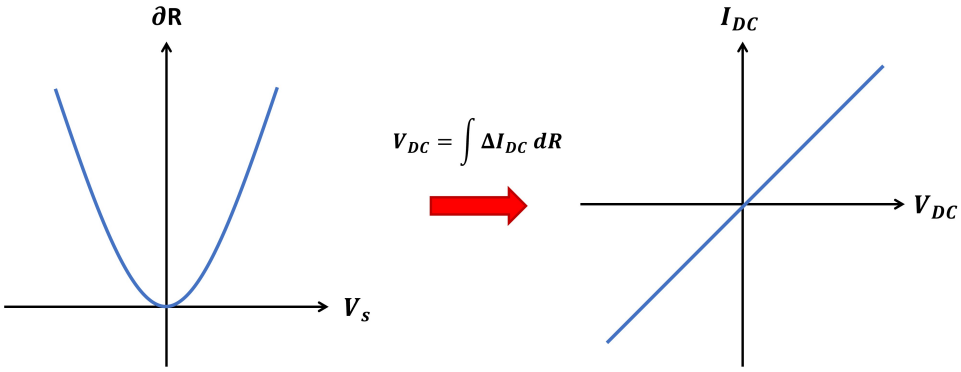

Figure 5.12: Sketch of the process to translate the differential resistance (dR) into the IV-characteristic through calculations described above.

6

Results and Discussions

Building upon the theoretical framework established in the previous chapters, this chapter presents and discusses the experimental results. The discussion is divided into two parts. The first part focuses on the YBCO nanowires with $t = 50$ nm, which have properties similar to the bulk YBCO including isotropic Fermi surface. In the second part, the preliminary results of the measurements on nanowires with $t = 10$ nm, the thickness that displays an anisotropic Fermi surface — a distinctive indication of electronic nematicity - are presented. The nanowires are slightly overdoped ($p \approx 0.19$). The purpose is to maintain the doping near the optimally doped and, at the same time, mitigate the effect of oxygen out-diffusion.

6.1 Results for the $t = 50$ nm

6.1.1 Probes on the Nanowires

Ideally, it is preferable to measure the YBCO nanowires at the lowest achievable temperature, while ensuring that the data can be observed within the normal states or slightly above the T_c. The low temperature is necessary because the effect of the Kapitza conductance is suppressed as temperature decreases. Hence, the first set of measurements was done near the liquid nitrogen temperature (~ 82 K). The IV curve of the nanowires with $L = 10$ μm and the voltage probes placed on the wires is shown in **Figure 6.1(a)**, and the corresponding $R(T)$ of the wires are shown in **Figure 6.1(b)**. The $R(P)$ and $T(P)$ were extracted from the methods discussed in the previous chapter. From Figure **Figure 6.1(d)**, it is evidenced that the $T(P)$ profile of the nanowires along the *a*- and *b*-axis are very identical and exhibit a linear trend except at low power. This deviation from linearity is due to the switching from the superconducting to the normal state. The linear $T(P)$ suggests that the Kapitza conductance strongly dominates the temperature profile. It is also shown that the Kapitza conductance is similar for both a- and b-axis-oriented nanowires.

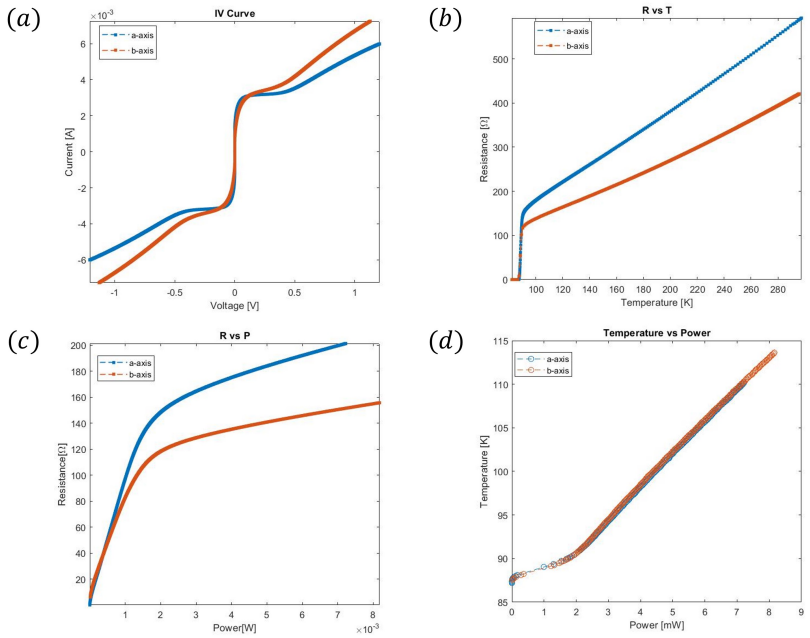

Figure 6.1: (a) and (b) displays the current-voltage (IV) characteristic and $R(T)$ of the YBCO nanowires with $L = 10\mu$m. The derived resistance vs. power ($R(P)$) is depicted in (c), whereas (d) shows the temperature vs. power ($T(P)$) data obtained by relating the resistance from (b) to (c).

To investigate the nature of e-ph coupling, it is crucial to also examine the low-power limit of the $T(P)$ data. However, the data at low power is obscured by the switching of the nanowires, making such observations impractical. The experiments were then carried out across a range of temperatures above T_c, from 300 K down to 110 K (close to the transition temperature). Examples of the $T(P)$ at $T = 300$ K and $T = 110$ K are shown in **Figure 6.2**. For both temperatures, it is shown that the $T(P)$ profiles are very similar and mostly linear, consistent with previous findings. According to the Figure, the thermal conductivity values for both *a*- and *b*-axis oriented wires are similar to the reported Kapitza conductivity values [120]. This indicates that the Kapitza conductance dominates the heating profile of the nanowires. It is worth mentioning that the step-like profile in **Figure 6.2(b)** is due to the measurement system. It is suspected that the behaviour is caused by the switching of the voltage scanning range in the function generator.

To further evaluate the heating transport, the statistical data for nanowires with different lengths and orientations are performed at different temperatures. The data comparison of the thermal conductivity between the nanowires with $L = 5\,\mu$m oriented in different directions are shown in **Figure 6.3(a)**. The statistical data demonstrates that the thermal conductivity values of both *a*-axis and *b*-axis nanowires are similar. The statistical data collected for the *b*-axis nanowires with different lengths, specifically $L = 5\,\mu$m and $10\,\mu$m, reveals similar thermal conductivity values, as depicted in **Figure 6.3(b)**. This observation suggests that nanowires with varying lengths exhibit comparable heat transport behavior, as long as the effect of thermal relaxation is negligible. Considering this factor, we can reasonably infer that the results shown in Figure **Figure 6.3(a)** would also apply to nanowires with $L \geq 5\,\mu$m. Nevertheless, the domination of the Kapitza conductance prevents the observation of the e-ph coupling.

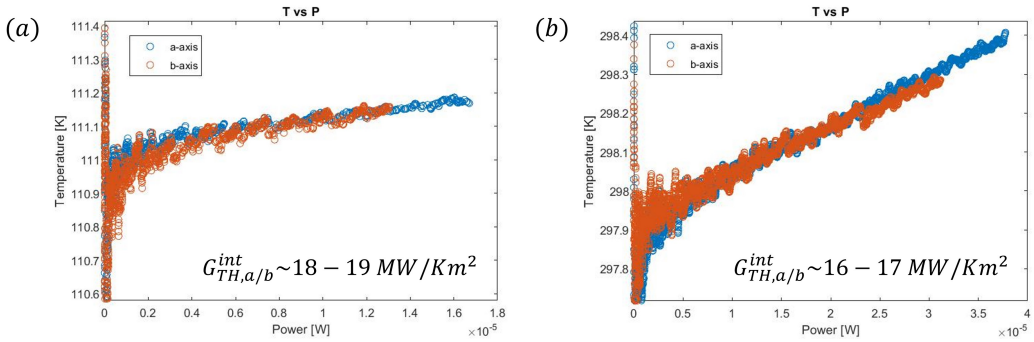

Figure 6.2: The comparison of $T(P)$ of the a- and b-axis oriented nanowires with $L = 10\,\mu$m measured at (a) 300 K and (b) 110 K. The maximum bias current was about 0.4 mA.

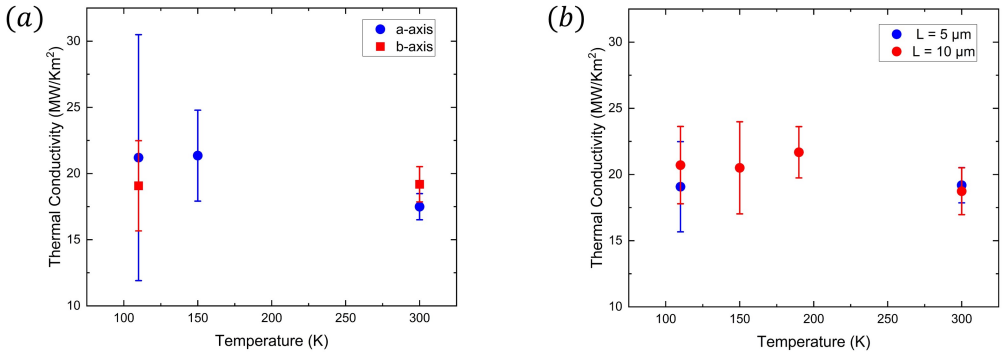

Figure 6.3: The statistical data of the thermal conductivity (MW/Km^2) that compares (a) the nanowires oriented along the different directions with $L = 5\,\mu$m and (b) the nanowires with different lengths.

Up to this point, we have observed two distinct disadvantages of using the DC measurement setup. Firstly, as previously mentioned, the data obtained at lower power is masked by significant noise making it impossible to accurately analyze the data. The second disadvantage is a large error bar in the data as evidenced by the statistical analysis (**Figure 6.3**). The Lock-In measurements were employed to address these issues. A comparative analysis between the DC and Lock-In measurements is shown in **Figure 6.4**, where each line represents each quadrant of the triangular signal. Figure **Figure 6.4(a)** illustrates that the signals obtained from the Lock-In exhibit significantly reduced noise and demonstrate close alignment with each other. Moreover, these signals effectively reveal the data even at extremely low power, a remarkable contrast to the DC measurement as shown in **Figure 6.4(b)**. Overall, the Lock-In measurement provides much more accurate results than the DC measurement. Due to its superiority, the Lock-In measurement will be the primary method utilized for the data analysis.

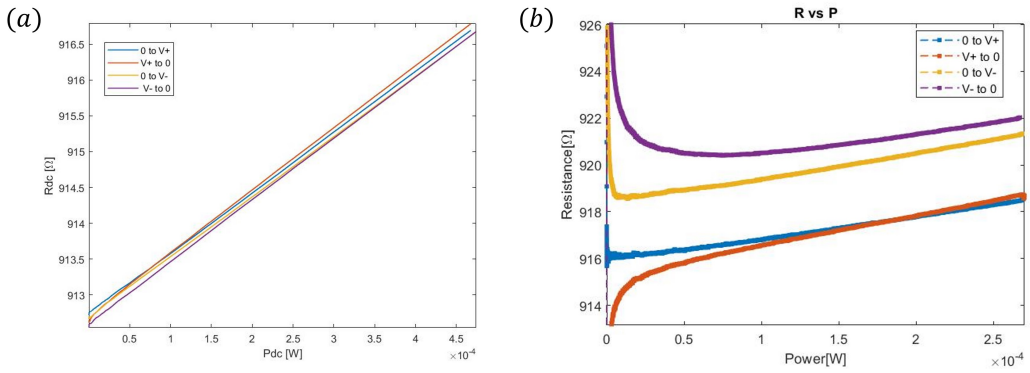

Figure 6.4: The comparison of the R(P) from (a) Lock-In and (b) DC measurement setup from the same nanowire.

6.1.2 Probes on the Electrodes

Due to the issues encountered with the measurement of the nanowires, we decided to move the probes to the electrode instead (see **Figure 5.7(b)** for the illustration) due to the following reasons. According to the simulation results, the effect of the heat diffusion from the wires into the electrode can be neglected for the nanowires with $L \geq 5$ μm. To observe such effects, only the interface area of the nanowire is used to calculate the total thermal conductivity. From previous measurements, the values of the Kapitza conductivity are expected to be below 25 MW/Km^2. Then, the effect of heat diffusion into electrodes can be observed if the total thermal conductivity exceeds such value. The temperature-dependent thermal conductivity of nanowires with different lengths and orientations are shown in **Figure 6.5**, while **Figure 6.6** shows direct comparisons of the thermal conductivity between a- and b-axis oriented nanowires at the same length.

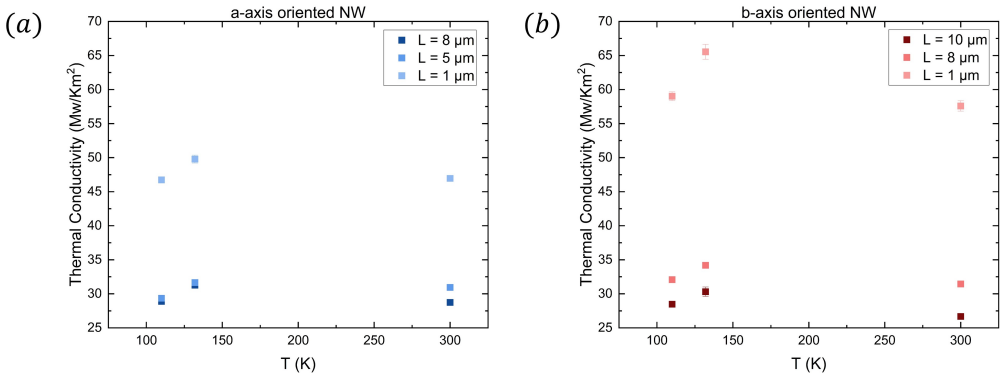

Figure 6.5: The temperature dependence of the total thermal conductivity of (a) a-axis and (b) b-axis oriented YBCO nanowires with different lengths.

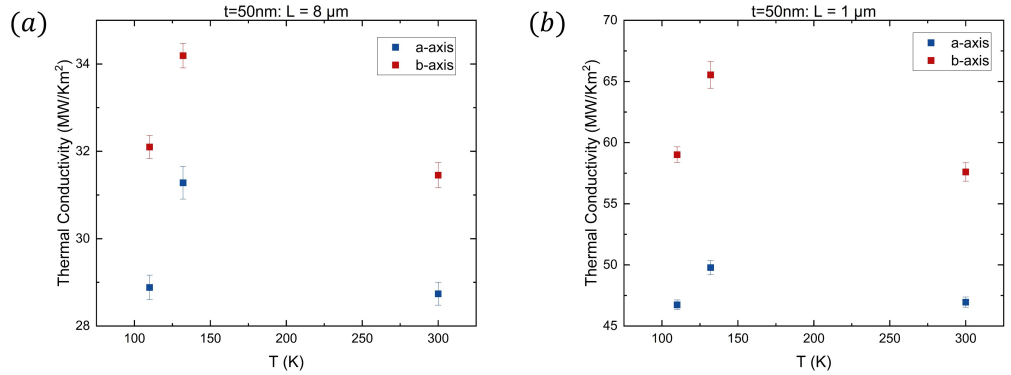

Figure 6.6: The temperature dependence of the total thermal conductivity that compares a- and b-axis oriented YBCO nanowires with (a) $L = 8\,\mu$m and (b) $L = 1\,\mu$m.

The total thermal conductivity of the a- and b-axis oriented YBCO nanowires are quite similar for the wires with $L \geq 5\,\mu$m, length scale where the contribution from the heat diffusion into electrodes is weak and the heat transport is dominated by out-of-plane (interface) component. The thermal conductivity along the b-axis is slightly higher than along the a-axis, which could be due to the CuO chains that align mostly along the b-axis. Hence, the results indicate the isotropic heat transport properties in the 50 nm thick nanowires. However, the thermal conductivity increases drastically when the wire is only $L = 1\,\mu$m long, confirming that the heat diffusion into electrodes has a great effect on the temperature profile of the short nanowires. The length-dependency of the thermal conductivity also indicates that the effect of the heat diffusion is stronger in the b-axis oriented nanowires, which could also be due to the contributions from CuO chains. Another noticeable feature is that the temperature-dependence trend of the thermal conductivity is the same for all nanowires: slightly increases when approaching 130 K and then slowly decreases when approaching 300 K. The reason is still unknown because the interface thermal conductivity is expected to be constant at higher temperatures (e.g., see [121] and [122]. Therefore, further investigation is required to determine the origin of the temperature dependency. The $T(P)$ measured at 110 K for $L = 8\,\mu$m nanowires are shown in **Figure 6.7**, which further confirms the linear $T(P)$ behaviour down to low power limit. It is noted that the deviation from linearity near zero power is due to the error in the lock-in measurements at the zero voltage offset limit.

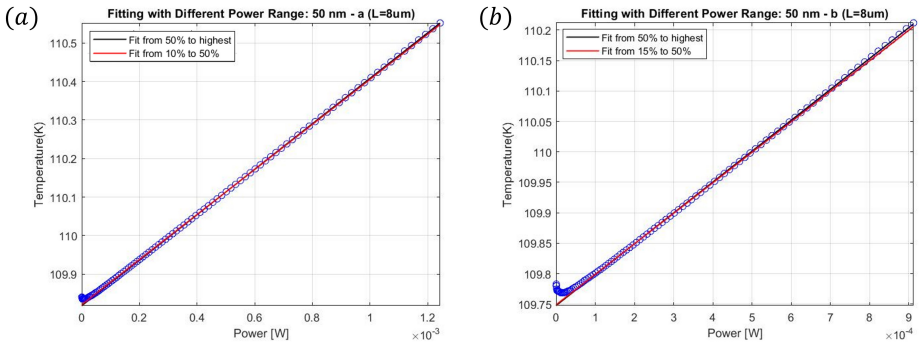

Figure 6.7: The $T(P)$ of 50 nm thick YBCO nanowires measured at 110 K with $L = 8\,\mu$m. The fittings are done at lower and higher power ranges to observe the linearity of the $T(P)$.

The following are the key takeaways from the results. Firstly, the Kapitza conductance strongly dominates the heat transport, as evidenced by the fact that the linearity of $T(P)$ is observed in all measurements. This is as expected since the effect of the Kapitza conductivity strongly dominates the e-ph coupling inside the materials at higher temperatures. Ideally, one would need to perform the measurements at very low temperatures (e.g., below 1-2 K [119] to better observe the e-ph coupling effects. Since the e-ph scattering is enhanced in a thinner structure, it might be possible to observe the effect of e-ph coupling in the $t = 10$ nm nanowires. Another concern is the real temperature dependency of the strange metal, which has not been properly studied. In this study, we assumed that the power-law dependency of normal metals can be applied to strange metals. If this is not the case, then it would be challenging to separate the e-ph coupling effects from the Kapitza conductivity. Nonetheless, the results provide a good approximation of the Kapitza conductivity between YBCO and MgO.

6.2 Results for the $t = 10$ nm

According to the heat transport model (see **Appendix A**), the interface conductivity should scale only with the interface area, while the e-ph coupling effect should be enhanced with decreasing film thickness. For direct comparisons, the nanowires were fabricated with the same geometry as the 50 nm thick nanowires and the same interface area was used to calculate the thermal conductivity. However, the actual behaviour deviates from the expectation. The results of the thermal conductivity measurement of the 10 nm thick YBCO nanowires oriented along the a- and b-axis are shown in **Figure 6.8**. The extracted thermal conductivity shows a similar temperature dependency as the 50 nm thick YBCO nanowires and the thermal conductivity along the b-axis is also slightly higher than the a-axis. Furthermore, the value of thermal conductivity for long wires increases more than a factor of five when compared to the 50 nm thick nanowires. In addition, the $T(P)$ measured at 110 K (**Figure 6.9**) shows no sign of deviation from linearity as well.

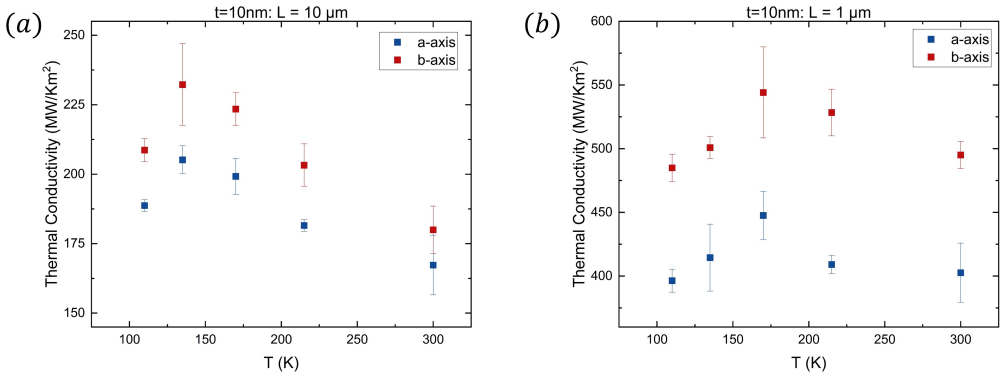

Figure 6.8: Total thermal conductivity vs. temperature of a- and b-axis oriented ultrathin YBCO nanowires with (a) $L = 10\,\mu$m and (b) $L = 1\,\mu$m.

According to the thermal conductivity values and the $T(P)$ characteristic, we can conclude that the effect of anisotropic e-ph coupling cannot be observed. The main speculation for the issues related to the anisotropy is that the thin film has a lower

anisotropy resistivity ratio than expected ($\frac{\rho_a}{\rho_b} \sim 1.5$, same as 50 nm thick nanowires), as reflected in **Figure 6.10**. Moreover, the difference in the slope of the T-linear resistivity of the a- and b-axis is similar to the 50 nm thick nanowires, suggesting that the nematic phase is weak. The information from the $R(T)$ confirms a lack of strong anisotropy in the measured ultrathin YBCO nanowires. Then, new ultrathin films with stronger $R(T)$ anisotropy are required for a proper study.

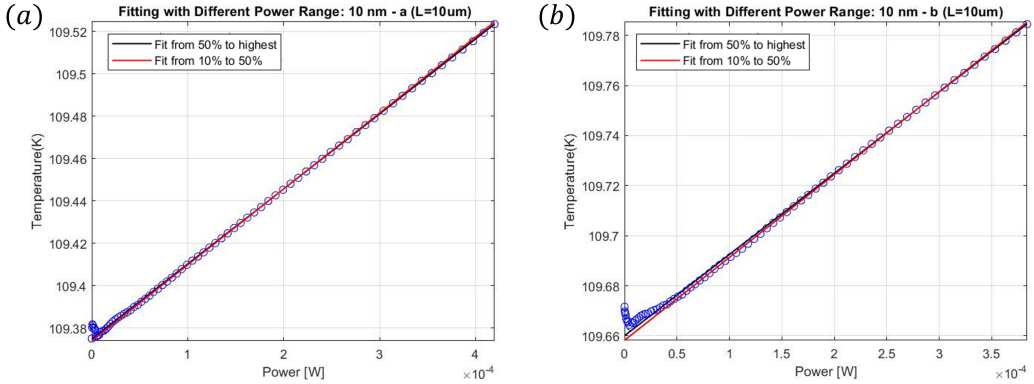

Figure 6.9: The $T(P)$ of 10 nm thick YBCO nanowires measured at 110 K with $L = 8\,\mu$m

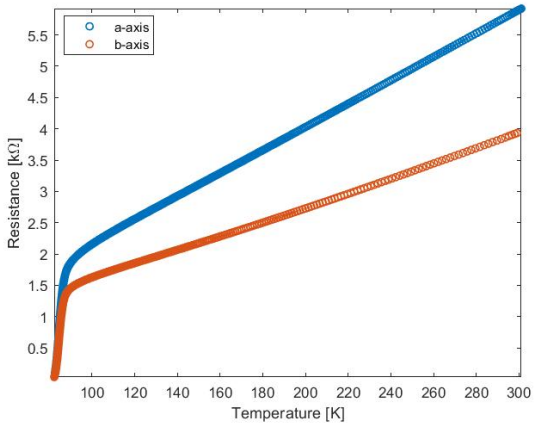

Figure 6.10: $R(T)$ of the 10 nm thick YBCO nanowires oriented along the a- and b-axis with $L = 10\,\mu$m.

The heat transport model (**Appendix A**) based on the series of thermal resistors shown in **Figure 5.1** cannot explain the drastic increase in thermal conductivity when reducing the thickness from 50 to 10 nm. Since the scaling of the thermal conductivity is proportional to the thickness reduction factor, there should be another heat conduction channel that is strongly affected by strong dimensional confinement in ultrathin films. One possibility for an extra channel is the coupling between YBCO's electrons and the substrate's phonons, referred to as electronic Kapitza conductance. According to the photoresponse [123, 124] and stationary [122] measurements of thicker YBCO films (e.g., 35 to 400 nm), the values of the interface conductivity converge to 20 MW/Km^2 which is also in agreement with our result (**Section 6.1.1**). However, the photoresponse measurements on ultrathin films (thickness less than 15 nm) indicate that the thermal

conductivity of the YBCO ultrathin films is enhanced by an order of magnitude compared to the thicker films [125, 126]. The results from [126] suggest the presence of electronic Kapitza conductivity. The total heat conduction channels then can be visualized according to **Figure 6.11**. Only ultrathin YBCO structures can feel this effect because it exists only at the interface between YBCO and the substrate. This would answer why the total thermal conductivity of 10 nm thick YBCO nanowires is at least a factor of five higher than the 50 nm thick nanowires. However, we still lack fine thickness-dependence data to confirm the existence of the electronic Kapitza conductivity.

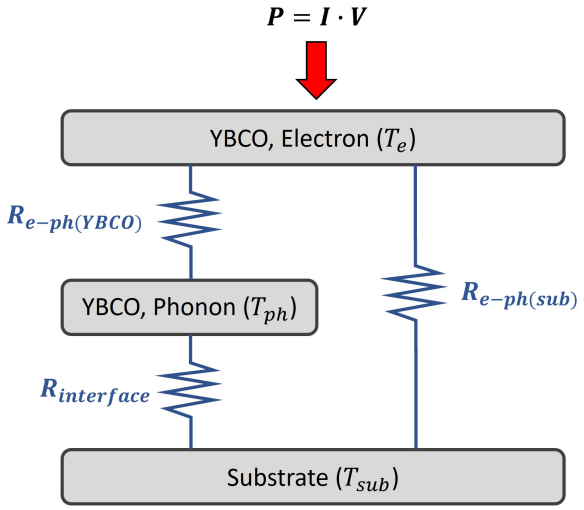

Figure 6.11: The thermal resistance model of the YBCO nanowire with electronic Kapitza conductance.

7

Conclusion and Future Outlook

The focus of this thesis is on the investigation of the e-ph coupling effects in strained YBCO nanowires through the study of electrical and heat transport measurements. To study the effect of strain on the YBCO nanostructures, two different thicknesses were selected for the comparison: 1) t=50 nm, where the properties of the YBCO are similar to the bulk material, and 2) t=10 nm (ultrathin), where it has been shown that the strain would results in the anisotropic Fermi surface, signaling the stabilization of the nematic phase.

The first part of this work focuses on the t=50 nm YBCO nanowires. We discovered that the heat transport is similar along the in-plane crystallographic directions. This behaviour aligns with our expectation for the YBCO with isotropic Fermi surface. However, heat transport is strongly dominated by interface conductivity. This was evidenced by the fact that the values of the total thermal conductivity, measured over a wide range of temperatures, strongly align with the reported interface conductivity for YBCO/MgO.

For the ultrathin nanowires, the extracted thermal conductivity also shows the same trend as the 50 nm thick nanowires. Two possible conclusions can be made. Firstly, a drastic increase in thermal conductivity could be caused by another heat dissipation channel that shows a strong effect only in ultrathin YBCO structures. A possible candidate is the electronic Kapitza resistance, where the electronic system inside the YBCO couples with the substrate's phonon at the interface. Secondly, the anisotropy is not strong enough to properly observe the effect of anisotropic e-ph coupling, as reflected in the thermal conductivity trends.

The following are possible outlooks for future work from this thesis:

- To confirm the presence of electronic Kapitza conductivity, the measurements of the T-dependent thermal conductivity of nanowires with intermediate thickness between 10 and 50 nm are required. Assuming that a drastic increase in thermal conductivity is caused by the electronic Kapitza conductance, the effect should be minimized after a certain thickness in the intermediate region.
- More information related to the Kapitza conductance can be extracted by studying how the substrate heats up when the nanowires are heated. Then, it is necessary to probe the substrate temperature by using the small nanowires as local thermometers. The example of the thermometers is shown in **Figure 4.2(b)**.
- Although the electronic Kapitza conductivity would mask the e-ph coupling effect in YBCO, further study of the ultrathin YBCO nanowires/films should provide some hints of the electronic nematic phase. According to the recent theoretical model [127] which attempts to explain the origin of the nematic Fermi surface observed in [34], the film-substrate coupling for YBCO is strongly dependent on the substrate's surface morphology. The key ingredient to obtain nematic Fermi surface lies in the elongated nanofacets with a triangular profile on the annealed MgO(110) surface. The strength of the coupling between YBCO adatoms and

MgO surface atoms differs depending on where the adatoms land and the coupling strength is the strongest on the nanofacets' edges. Hence, the nanofacets on the MgO surface result in a strongly anisotropic strain on the YBCO atomic structure at the interface, which gives rise to a nematic Fermi surface where the electronic states are suppressed along the same direction that the MgO nanofacets align. Although the model correctly predicts the presence of the nematic Fermi surface of the underdoped ultrathin YBCO ($p \sim 0.12$), it also predicts that the Fermi surface becomes isotropic again while maintaining the nematicity. Therefore, the heat transport measurement of the ultrathin YBCO nanowires with the doping level of $0.12 < p < 0.16$ should reveal more information regarding the presence of the nematic state. Additional insights into the presence of the could be obtained by systematically studying the CDW at the intermediate doping range (e.g., through RIXS experiments). Furthermore, the investigation of thin films with a thickness even thinner than 10 nm may yield intriguing findings as well.

- The heat transport model for the e-ph coupling in YBCO has been developed based on the normal metals where $T \propto P^{1/5}$. However, we have not observed any sign of the power-law dependency even at $T = 110$ K. To accurately probe the contribution from e-ph, we need to perform measurements at very low temperatures for better observation. Ideally, it would require us to completely remove the superconductivity by applying a magnetic field. However, the complete suppression of the superconducting order at the optimally doped is not feasible because the critical field is extremely high (approximately 100 T). Then, underdoped YBCO is preferable for the measurement due to lower critical temperature and critical magnetic field.
- This thesis mainly focuses on long nanowires, where the temperature profile across the nanowire is assumed to be stable. However, a complete simulation of the heat transport, including the heat dissipation from the nanowire into the electrodes and from the e-ph scattering, is required to accurately model the temperature profile in the nanowire.

Bibliography

[1] J. G. Bednorz and K. A. Müller, "Possible high T_c superconductivity in the Ba-La-Cu-O system," *Z. Phys. B Condens. Matter*, vol. 64, pp. 189–193, 1986.

[2] J. Bardeen, L. N. Cooper, and J. R. Schrieffer, "Theory of superconductivity," *Phys. Rev.*, vol. 108, p. 1175, 1957.

[3] A. Mourachkine, *Room-temperature superconductivity*. Cambridge Int Science Publishing, 2004.

[4] B. Lilia, R. Hennig, P. Hirschfeld, G. Profeta, A. Sanna, E. Zurek, W. E. Pickett, M. Amsler, R. Dias, M. I. Eremets, *et al.*, "The 2021 room-temperature superconductivity roadmap," *J. Phys. Condens. Matter.*, vol. 34, p. 183002, 2022.

[5] E. Morosan, D. Natelson, A. H. Nevidomskyy, and Q. Si, "Strongly correlated materials," *Adv. Mater.*, vol. 24, pp. 4896–4923, 2012.

[6] B. Keimer, S. A. Kivelson, M. R. Norman, S. Uchida, and J. Zaanen, "From quantum matter to high-temperature superconductivity in copper oxides," *Nature*, vol. 518, pp. 179–186, 2015.

[7] K. Chao, J. Spałek, and A. Oleś, "Canonical perturbation expansion of the Hubbard model," *Phys. Rev. B*, vol. 18, p. 3453, 1978.

[8] E. Carlson, S. Kivelson, D. Orgad, and V. Emery, "Concepts in high temperature superconductivity," *The Physics of Superconductors: Vol. II. Superconductivity in Nanostructures, High-T_c and Novel Superconductors, Organic Superconductors*, pp. 275–451, 2004.

[9] S. Sachdev and B. Keimer, "Quantum criticality," *Phys. Today*, vol. 64, pp. 29–35, 2011.

[10] J. Tahir-Kheli and W. Goddard 3rd, "Spinons and holons for the one-dimensional three-band hubbard models of high-temperature superconductors.," *Proc. Natl. Acad. Sci.*, vol. 90, pp. 9959–9962, 1993.

[11] J. Schrieffer, X. Wen, and S. Zhang, "Dynamic spin fluctuations and the bag mechanism of high-T_c superconductivity," *Phys. Rev. B*, vol. 39, p. 11663, 1989.

[12] B. Chakraverty and J. Ranninger, "Bipolarons and superconductivity," *Phil. Mag. B.*, vol. 52, pp. 669–678, 1985.

[13] P. W. Anderson, "The resonating valence bond state in La_2CuO_4 and superconductivity," *Science*, vol. 235, pp. 1196–1198, 1987.

[14] E. Fradkin, S. A. Kivelson, and J. M. Tranquada, "Colloquium: Theory of intertwined orders in high temperature superconductors," *Rev. Mod. Phys.*, vol. 87, p. 457, 2015.

[15] J. Zaanen, "Planckian dissipation, minimal viscosity and the transport in cuprate strange metals," *SciPost Phys.*, vol. 6, p. 061, 2019.

[16] P. W. Phillips, N. E. Hussey, and P. Abbamonte, "Stranger than metals," *Science*, vol. 377, p. eabh4273, 2022.

[17] C. Proust and L. Taillefer, "The remarkable underlying ground states of cuprate superconductors," *Annu. Rev. Condens. Matter Phys.*, vol. 10, pp. 409–429, 2019.

[18] S. Sachdev and S.-C. Zhang, "Tuning order in cuprate superconductors," *Science*, vol. 295, pp. 452–454, 2002.

[19] J. Chang, C. Niedermayer, R. Gilardi, N. Christensen, H. M. Rønnow, D. McMorrow, M. Ay, J. Stahn, O. Sobolev, A. Hiess, *et al.*, "Tuning competing orders in $La_{2-x}Sr_xCuO_4$ cuprate superconductors by the application of an external magnetic field," *Phys. Rev. B*, vol. 78, p. 104525, 2008.

[20] E. Wahlberg, R. Arpaia, G. Seibold, M. Rossi, R. Fumagalli, E. Trabaldo, N. B. Brookes, L. Braicovich, S. Caprara, U. Gran, G. Ghiringhelli, T. Bauch, and F. Lombardi, "Restored strange metal phase through suppression of charge density waves in underdoped $YBa_2Cu_3O_{7-\delta}$," *Science*, vol. 373, pp. 1506–1510, 2021.

[21] T. Devereaux, T. Cuk, Z.-X. Shen, and N. Nagaosa, "Anisotropic electron-phonon interaction in the cuprates," *Phys. Rev. Lett.*, vol. 93, p. 117004, 2004.

[22] H. K. Onnes, "The resistance of pure mercury at helium temperatures. further experiments with liquid helium. IV," in *Proceedings Koninklijke Akademie van Wetenschappen te Amsterdam*, vol. 13, pp. 1274–1276, 1911.

[23] W. Meissner and R. Ochsenfeld, "Ein neuer effekt bei eintritt der supraleitfähigkeit," *Sci. Nat.*, vol. 21, pp. 787–788, 1933.

[24] F. London and H. London, "The electromagnetic equations of the supraconductor," *Proc. R. Soc. Lond.*, vol. 149, pp. 71–88, 1935.

[25] V. L. Ginzburg, V. L. Ginzburg, and L. Landau, *On the theory of superconductivity*. Springer, 2009.

[26] A. A. Abrikosov, "On the magnetic properties of superconductors of the second group," *Sov. Phys. J. Exp. Theor. Phys.*, vol. 5, pp. 1174–1182, 1957.

[27] E. Maxwell, "Isotope effect in the superconductivity of mercury," *Phys. Rev.*, vol. 78, p. 477, 1950.

[28] H. Fröhlich, "Theory of the superconducting state. I. the ground state at the absolute zero of temperature," *Phys. Rev.*, vol. 79, p. 845, 1950.

[29] J. Bardeen, "Zero-point vibrations and superconductivity," *Phys. Rev.*, vol. 79, p. 167, 1950.

[30] J. Bardeen, L. N. Cooper, and J. R. Schrieffer, "Microscopic theory of superconductivity," *Phys. Rev.*, vol. 106, p. 162, 1957.

[31] J. Bardeen, L. N. Cooper, and J. R. Schrieffer, "Theory of superconductivity," *Phys. Rev.*, vol. 108, p. 1175, 1957.

[32] W. McMillan, "Transition temperature of strong-coupled superconductors," *Phys. Rev.*, vol. 167, p. 331, 1968.

[33] M.-K. Wu, J. R. Ashburn, C. Torng, P.-H. Hor, R. L. Meng, L. Gao, Z. J. Huang, Y. Wang, and a. Chu, "Superconductivity at 93 K in a new mixed-phase Y-Ba-Cu-O compound system at ambient pressure," *Phys. Rev. Lett.*, vol. 58, p. 908, 1987.

[34] E. Wahlberg, *Reshaping the Phase Diagram of $YBa_2Cu_3O_{7-\delta}$ Through Strain in Ultrathin Films and Nanowires*. Chalmers Tekniska Hogskola (Sweden), 2021.

[35] C. Namgung, J. Irvine, J. Binks, and A. West, "Orthorhombic-tetragonal transition in $YBa_2Cu_3O_x$," *Supercond. Sci. Technol.*, vol. 1, p. 169, 1988.

[36] J. Jorgensen, B. Veal, A. P. Paulikas, L. Nowicki, G. Crabtree, H. Claus, and W. Kwok, "Structural properties of oxygen-deficient $YBa_2Cu_3O_{7-\delta}$," *Phys. Rev. B*, vol. 41, p. 1863, 1990.

[37] R. Liang, D. Bonn, and W. Hardy, "Evaluation of CuO_2 plane hole doping in $YBa_2Cu_3O_{6+x}$ single crystals," *Phys. Rev. B*, vol. 73, p. 180505, 2006.

[38] J. Ye and K. Nakamura, "Quantitative structure analyses of $YBa_2Cu_3O_{7-\delta}$ thin films: Determination of oxygen content from x-ray-diffraction patterns," *Phys. Rev. B*, vol. 48, p. 7554, 1993.

[39] J. R. Waldram, *Superconductivity of metals and cuprates*. CRC Press, 1996.

[40] B. T. Matthias, T. H. Geballe, and V. B. Compton, "Superconductivity," *Rev. Mod. Phys.*, vol. 35, pp. 1–22, 1963.

[41] J. Eisenstein, "Superconducting elements," *Rev. Mod. Phys.*, vol. 26, p. 277, 1954.

[42] C. Tsuei and J. Kirtley, "Pairing symmetry in cuprate superconductors," *Rev. Mod. Phys.*, vol. 72, p. 969, 2000.

[43] M. Okawa, K. Ishizaka, H. Uchiyama, H. Tadatomo, T. Masui, S. Tajima, X.-Y. Wang, C.-T. Chen, S. Watanabe, A. Chainani, *et al.*, "Superconducting electronic state in optimally doped $YBa_2Cu_3O_{7-\delta}$ observed with laser-excited angle-resolved photoemission spectroscopy," *Phys. Rev. B*, vol. 79, p. 144528, 2009.

[44] T. Devereaux, T. Cuk, Z.-X. Shen, and N. Nagaosa, "Anisotropic electron-phonon interaction in the cuprates," *Phys. Rev. Lett.*, vol. 93, p. 117004, 2004.

[45] X. Zhou, J. Hussain, and Z.-X. Shen, "Technical Reports: Electron-Phonon Coupling in High-Temperature Cuprate Superconductors as Revealed by Angle-Resolved Photoemission Spectroscopy," *Synchrotron Radiat. News*, vol. 18, pp. 15–23, 2005.

[46] L. Braicovich, M. Rossi, R. Fumagalli, Y. Peng, Y. Wang, R. Arpaia, D. Betto, G. M. De Luca, D. Di Castro, K. Kummer, M. Moretti Sala, M. Pagetti, G. Balestrino, N. B. Brookes, M. Salluzzo, S. Johnston, J. van den Brink,

and G. Ghiringhelli, "Determining the electron-phonon coupling in superconducting cuprates by resonant inelastic x-ray scattering: Methods and results on $Nd_{1+x}Ba_{2-x}Cu_3O_{7-\delta}$," *Phys. Rev. Research*, vol. 2, p. 023231, 2020.

[47] A.-M. Zhang and Q.-M. Zhang, "Electron—phonon coupling in cuprate and iron-based superconductors revealed by raman scattering," *Chin. Phys. B*, vol. 22, p. 087103, 2013.

[48] N. J. Jabusch, P. Dayal, and A. F. Kemper, "Catalogue of phonon modes in several cuprate high-temperature superconductors from density functional theory," *SciPost Phys. Core*, vol. 6, p. 018, 2023.

[49] S. Johnston, F. Vernay, B. Moritz, Z.-X. Shen, N. Nagaosa, J. Zaanen, and T. Devereaux, "Systematic study of electron-phonon coupling to oxygen modes across the cuprates," *Phys. Rev. B*, vol. 82, p. 064513, 2010.

[50] R. Abd-Shukor, "Electron–phonon coupling constant of cuprate based high temperature superconductors," *Solid State Commun.*, vol. 142, pp. 587–590, 2007.

[51] Y. Peng, L. Martinelli, Q. Li, M. Rossi, M. Mitrano, R. Arpaia, M. M. Sala, Q. Gao, X. Guo, G. M. De Luca, *et al.*, "Doping dependence of the electron-phonon coupling in two families of bilayer superconducting cuprates," *Phys. Rev. B*, vol. 105, p. 115105, 2022.

[52] C. Jiang, M. Baggioli, E. Liarokapis, and A. Zaccone, "Correlation between optical phonon softening and superconducting T_c in $YBa_2Cu_3O_x$," *arXiv preprint arXiv:2306.05763*, 2023.

[53] S. Banerjee, W. Atkinson, and A. P. Kampf, "Emergent charge order from correlated electron-phonon physics in cuprates," *Commun. Phys.*, vol. 3, p. 161, 2020.

[54] Y. Li, W. Liang, N. Li, Y. Chen, S. Luo, and Y. Zhao, "Correlation of pseudogap, superconducting ordering and superconducting fluctuations with electron–phonon interactions in $Bi_2Sr_2CaCu_2O_{8+\delta}$," *New J. Phys.*, vol. 24, p. 033023, 2022.

[55] T. Das and C. Panagopoulos, "Two types of superconducting domes in unconventional superconductors," *New J. Phys.*, vol. 18, p. 103033, 2016.

[56] P. A. Lee, N. Nagaosa, and X.-G. Wen, "Doping a Mott insulator: Physics of high-temperature superconductivity," *Rev. Mod. Phys.*, vol. 78, p. 17, 2006.

[57] D. Haug, V. Hinkov, Y. Sidis, P. Bourges, N. B. Christensen, A. Ivanov, T. Keller, C. Lin, and B. Keimer, "Neutron scattering study of the magnetic phase diagram of underdoped $YBa_2Cu_3O_{6+x}$," *New J. Phys.*, vol. 12, p. 105006, 2010.

[58] M. Kofu, S.-H. Lee, M. Fujita, H.-J. Kang, H. Eisaki, and K. Yamada, "Hidden quantum spin-gap state in the static stripe phase of high-temperature $La_{2-x}Sr_xCuO_4$ superconductors," *Phys. Rev. Lett.*, vol. 102, p. 047001, 2009.

[59] S. Badoux, S. Afshar, B. Michon, A. Ouellet, S. Fortier, D. LeBoeuf, T. Croft, C. Lester, S. Hayden, H. Takagi, *et al.*, "Critical doping for the onset of fermi-surface reconstruction by charge-density-wave order in the cuprate superconductor $La_{2-x}Sr_xCuO_4$," *Phys. Rev. X*, vol. 6, p. 021004, 2016.

[60] S. Lee, E. W. Huang, T. A. Johnson, X. Guo, A. A. Husain, M. Mitrano, K. Lu, A. V. Zakrzewski, G. A. de la Peña, Y. Peng, *et al.*, "Generic character of charge and spin density waves in superconducting cuprates," *Proc. Natl. Acad. Sci.*, vol. 119, p. e2119429119, 2022.

[61] K. M. Shen, F. Ronning, D. Lu, F. Baumberger, N. Ingle, W. Lee, W. Meevasana, Y. Kohsaka, M. Azuma, M. Takano, *et al.*, "Nodal quasiparticles and antinodal charge ordering in $Ca_{2-x}Na_xCuO_2Cl_2$," *Science*, vol. 307, pp. 901–904, 2005.

[62] D. Marshall, D. Dessau, A. Loeser, C. Park, A. Matsuura, J. Eckstein, I. Bozovic, P. Fournier, A. Kapitulnik, W. Spicer, *et al.*, "Unconventional electronic structure evolution with hole doping in $Bi_2Sr_2CaCu_2O_{8+\delta}$: Angle-resolved photoemission results," *Phys. Rev. Lett.*, vol. 76, p. 4841, 1996.

[63] K. Tanaka, W. Lee, D. Lu, A. Fujimori, T. Fujii, Risdiana, I. Terasaki, D. Scalapino, T. Devereaux, Z. Hussain, *et al.*, "Distinct fermi-momentum-dependent energy gaps in deeply underdoped Bi2212," *Science*, vol. 314, pp. 1910–1913, 2006.

[64] S. Badoux, W. Tabis, F. Laliberté, G. Grissonnanche, B. Vignolle, D. Vignolles, J. Béard, D. Bonn, W. Hardy, R. Liang, *et al.*, "Change of carrier density at the pseudogap critical point of a cuprate superconductor," *Nature*, vol. 531, pp. 210–214, 2016.

[65] S.-D. Chen, M. Hashimoto, Y. He, D. Song, K.-J. Xu, J.-F. He, T. P. Devereaux, H. Eisaki, D.-H. Lu, J. Zaanen, *et al.*, "Incoherent strange metal sharply bounded by a critical doping in Bi2212," *Science*, vol. 366, pp. 1099–1102, 2019.

[66] O. Cyr-Choinière, R. Daou, F. Laliberté, C. Collignon, S. Badoux, D. LeBoeuf, J. Chang, B. Ramshaw, D. Bonn, W. Hardy, *et al.*, "Pseudogap temperature T* of cuprate superconductors from the nernst effect," *Phys. Rev. B*, vol. 97, p. 064502, 2018.

[67] M. R. Norman, H. Ding, M. Randeria, J. C. Campuzano, T. Yokoya, T. Takeuchi, T. Takahashi, T. Mochiku, K. Kadowaki, P. Guptasarma, *et al.*, "Destruction of the fermi surface in underdoped high-T_c superconductors," *Nature*, vol. 392, pp. 157–160, 1998.

[68] W. Jiang, Y. Liu, A. Klein, Y. Wang, K. Sun, A. V. Chubukov, and Z. Y. Meng, "Monte carlo study of the pseudogap and superconductivity emerging from quantum magnetic fluctuations," *Nat. Commun.*, vol. 13, p. 2655, 2022.

[69] M. Zhu, D. Voneshen, S. Raymond, O. Lipscombe, C. Tam, and S. Hayden, "Spin fluctuations associated with the collapse of the pseudogap in a cuprate superconductor," *Nat. Phys.*, vol. 19, pp. 99–105, 2023.

[70] S. Hüfner, M. Hossain, A. Damascelli, and G. Sawatzky, "Two gaps make a high-temperature superconductor?," *Rep. Prog. Phys.*, vol. 71, p. 062501, 2008.

[71] J. Chang, E. Blackburn, A. Holmes, N. B. Christensen, J. Larsen, J. Mesot, R. Liang, D. Bonn, W. Hardy, A. Watenphul, *et al.*, "Direct observation of competition between superconductivity and charge density wave order in $YBa_2Cu_3O_{6.67}$," *Nat. Phys.*, vol. 8, pp. 871–876, 2012.

[72] M. Huecker, N. B. Christensen, A. Holmes, E. Blackburn, E. M. Forgan, R. Liang,

D. Bonn, W. Hardy, O. Gutowski, M. v. Zimmermann, *et al.*, "Competing charge, spin, and superconducting orders in underdoped $YBa_2Cu_3O_y$," *Phys. Rev. B*, vol. 90, p. 054514, 2014.

[73] S. Blanco-Canosa, A. Frano, E. Schierle, J. Porras, T. Loew, M. Minola, M. Bluschke, E. Weschke, B. Keimer, and M. Le Tacon, "Resonant x-ray scattering study of charge-density wave correlations in $YBa_2Cu_3O_{6+x}$," *Phys. Rev. B*, vol. 90, p. 054513, 2014.

[74] P. Fournier, P. Mohanty, E. Maiser, S. Darzens, T. Venkatesan, C. Lobb, G. Czjzek, R. A. Webb, and R. Greene, "Insulator-metal crossover near optimal doping in $Pr_{2-x}Ce_xCuO_4$: Anomalous normal-state low temperature resistivity," *Phys. Rev. Lett.*, vol. 81, p. 4720, 1998.

[75] M. Gurvitch and A. Fiory, "Resistivity of $La_{1.825}Sr_{0.175}CuO_4$ and $YBa_2Cu_3O_7$ to 1100 K: absence of saturation and its implications," *Phys. Rev. Lett.*, vol. 59, p. 1337, 1987.

[76] G. Baym and C. Pethick, "Landau fermi-liquid theory: concepts and applications," 2008.

[77] N. Hussey, K. Takenaka, and H. Takagi, "Universality of the Mott–Ioffe–Regel limit in metals," *Phil. Mag.*, vol. 84, pp. 2847–2864, 2004.

[78] L. Chen, D. T. Lowder, E. Bakali, A. Andrews, W. Schrenk, M. Waas, R. Svagera, G. Eguchi, L. Prochaska, Q. Si, *et al.*, "Shot noise indicates the lack of quasiparticles in a strange metal," *Science*, vol. 382, pp. 907–911, 2023.

[79] A. Legros, S. Benhabib, W. Tabis, F. Laliberté, M. Dion, M. Lizaire, B. Vignolle, D. Vignolles, H. Raffy, Z. Li, *et al.*, "Universal T-linear resistivity and Planckian dissipation in overdoped cuprates," *Nat. Phys.*, vol. 15, pp. 142–147, 2019.

[80] S. Sachdev, "Where is the quantum critical point in the cuprate superconductors?," *Phys. Status Solidi B*, vol. 247, pp. 537–543, 2010.

[81] B. Michon, C. Girod, S. Badoux, J. Kačmarčík, Q. Ma, M. Dragomir, H. Dabkowska, B. Gaulin, J.-S. Zhou, S. Pyon, *et al.*, "Thermodynamic signatures of quantum criticality in cuprate superconductors," *Nature*, vol. 567, pp. 218–222, 2019.

[82] G. Seibold, R. Arpaia, Y. Y. Peng, R. Fumagalli, L. Braicovich, C. Di Castro, M. Grilli, G. C. Ghiringhelli, and S. Caprara, "Strange metal behaviour from charge density fluctuations in cuprates," *Commun. Phys.*, vol. 4, p. 7, 2021.

[83] R. Arpaia and G. Ghiringhelli, "Charge order at high temperature in cuprate superconductors," *J. Phys. Soc. Jpn.*, vol. 90, p. 111005, 2021.

[84] R. Arpaia, L. Martinelli, M. M. Sala, S. Caprara, A. Nag, N. B. Brookes, P. Camisa, Q. Li, Q. Gao, X. Zhou, M. Garcia-Fernandez, K.-J. Zhou, E. Schierle, T. Bauch, Y. Y. Peng, C. Di Castro, M. Grilli, F. Lombardi, L. Braicovich, and G. Ghiringhelli, "Signature of quantum criticality in cuprates by charge density fluctuations," *Nat. Commun.*, vol. 14, p. 7198, 2023.

[85] D. Di Sante, J. Erdmenger, M. Greiter, I. Matthaiakakis, R. Meyer, D. R. Fer-

nández, R. Thomale, E. van Loon, and T. Wehling, "Turbulent hydrodynamics in strongly correlated Kagome metals," *Nat. Commun.*, vol. 11, p. 3997, 2020.

[86] T. Kondo, W. Malaeb, Y. Ishida, T. Sasagawa, H. Sakamoto, T. Takeuchi, T. Tohyama, and S. Shin, "Point nodes persisting far beyond t_c in Bi2212," *Nat. Commun.*, vol. 6, p. 7699, 2015.

[87] J. Chang, M. Maansson, S. Pailhes, T. Claesson, O. Lipscombe, S. M. Hayden, L. Patthey, O. Tjernberg, and J. Mesot, "Anisotropic breakdown of Fermi liquid quasiparticle excitations in overdoped $La_{2-x}Sr_xCuO_4$," *Nat. Commun.*, vol. 4, p. 2559, 2013.

[88] Y. Peng, R. Fumagalli, Y. Ding, M. Minola, S. Caprara, D. Betto, M. Bluschke, G. De Luca, K. Kummer, E. Lefrançois, *et al.*, "Re-entrant charge order in overdoped $(Bi,Pb)_{2.12}Sr_{1.88}CuO_{6+\delta}$ outside the pseudogap regime," *Nat. Mater.*, vol. 17, pp. 697–702, 2018.

[89] R. Arpaia, E. Andersson, E. Trabaldo, T. Bauch, and F. Lombardi, "Probing the phase diagram of cuprates with $YBa_2Cu_3O_{7-\delta}$ thin films and nanowires," *Phys. Rev. Materials*, vol. 2, p. 024804, 2018.

[90] L. Sederholm, S. D. Conradson, T. H. Geballe, C.-Q. Jin, A. Gauzzi, E. Gilioli, M. Karppinen, and G. Baldinozzi, "Extremely overdoped superconducting cuprates via high pressure oxygenation methods," *Condens. Matter*, vol. 6, p. 50, 2021.

[91] A. Augieri, T. Petrisor, G. Celentano, L. Ciontea, V. Galluzzi, U. Gambardella, A. Mancini, and A. Rufoloni, "Effect of Ca doping in YBCO superconducting thin films," *Physica C*, vol. 401, pp. 320–324, 2004.

[92] S. Nakata, M. Horio, K. Koshiishi, K. Hagiwara, C. Lin, M. Suzuki, S. Ideta, K. Tanaka, D. Song, Y. Yoshida, *et al.*, "Nematicity in a cuprate superconductor revealed by angle-resolved photoemission spectroscopy under uniaxial strain," *npj Quantum Mater.*, vol. 6, p. 86, 2021.

[93] S. A. Kivelson, E. Fradkin, and V. J. Emery, "Electronic liquid-crystal phases of a doped mott insulator," *Nature*, vol. 393, pp. 550–553, 1998.

[94] J. Tranquada, B. Sternlieb, J. Axe, Y. Nakamura, and S. Uchida, "Evidence for stripe correlations of spins and holes in copper oxide superconductors," *Nature*, vol. 375, pp. 561–563, 1995.

[95] H.-H. Kuo, J.-H. Chu, J. C. Palmstrom, S. A. Kivelson, and I. R. Fisher, "Ubiquitous signatures of nematic quantum criticality in optimally doped Fe-based superconductors," *Science*, vol. 352, pp. 958–962, 2016.

[96] F. Ronning, T. Helm, K. Shirer, M. Bachmann, L. Balicas, M. K. Chan, B. Ramshaw, R. D. Mcdonald, F. F. Balakirev, M. Jaime, *et al.*, "Electronic in-plane symmetry breaking at field-tuned quantum criticality in $CeRhIn_5$," *Nature*, vol. 548, pp. 313–317, 2017.

[97] R. Tao, Y.-J. Yan, X. Liu, Z.-W. Wang, Y. Ando, Q.-H. Wang, T. Zhang, and D.-L. Feng, "Direct visualization of the nematic superconductivity in $Cu_xBi_2Se_3$," *Phys. Rev. X*, vol. 8, p. 041024, 2018.

[98] J. Wang, Y. Wu, X. Zhou, Y. Li, B. Teng, P. Dong, J. He, Y. Zhang, Y. Ding, and J. Li, "Progress of nematic superconductivity in iron-based superconductors," *Adv. Phys.: X*, vol. 6, p. 1878931, 2021.

[99] R. S. Markiewicz, J. Lorenzana, G. Seibold, and A. Bansil, "Short range smectic order driving long range nematic order: example of cuprates," *Sci. Rep.*, vol. 6, pp. 1–7, 2016.

[100] A. Fedorov, A. Yaresko, T. Kim, Y. Kushnirenko, E. Haubold, T. Wolf, M. Hoesch, A. Grüneis, B. Büchner, and S. Borisenko, "Effect of nematic ordering on electronic structure of FeSe," *Sci. Rep.*, vol. 6, pp. 1–7, 2016.

[101] S. Mukhopadhyay, R. Sharma, C. K. Kim, S. D. Edkins, M. H. Hamidian, H. Eisaki, S. Uchida, E.-A. Kim, M. J. Lawler, A. P. Mackenzie, *et al.*, "Evidence for a vestigial nematic state in the cuprate pseudogap phase," *Proc. Natl. Acad. Sci.*, vol. 116, pp. 13249–13254, 2019.

[102] Y. Ando, K. Segawa, S. Komiya, and A. Lavrov, "Electrical resistivity anisotropy from self-organized one dimensionality in high-temperature superconductors," *Phys. Rev. Lett.*, vol. 88, p. 137005, 2002.

[103] R. Daou, J. Chang, D. LeBoeuf, O. Cyr-Choiniere, F. Laliberté, N. Doiron-Leyraud, B. Ramshaw, R. Liang, D. Bonn, W. Hardy, *et al.*, "Broken rotational symmetry in the pseudogap phase of a high-T_c superconductor," *Nature*, vol. 463, pp. 519–522, 2010.

[104] Y. Sato, S. Kasahara, H. Murayama, Y. Kasahara, E.-G. Moon, T. Nishizaki, T. Loew, J. Porras, B. Keimer, T. Shibauchi, *et al.*, "Thermodynamic evidence for a nematic phase transition at the onset of the pseudogap in $YBa_2Cu_3O_y$," *Nat. Phys.*, vol. 13, pp. 1074–1078, 2017.

[105] R. Arpaia, M. Arzeo, R. Baghdadi, E. Trabaldo, F. Lombardi, and T. Bauch, "Improved noise performance of ultrathin YBCO dayem bridge nanosquids," *Supercond. Sci. Technol.*, vol. 30, p. 014008, 2016.

[106] E. Trabaldo, C. Pfeiffer, E. Andersson, R. Arpaia, A. Kalaboukhov, D. Winkler, F. Lombardi, and T. Bauch, "Grooved dayem nanobridges as building blocks of high-performance $YBa_2Cu_3O_{7-\delta}$ SQUID magnetometers," *Nano Lett.*, vol. 19, pp. 1902–1907, 2019.

[107] R. Arpaia, M. Ejrnaes, L. Parlato, F. Tafuri, R. Cristiano, D. Golubev, R. Sobolewski, T. Bauch, F. Lombardi, and G. P. Pepe, "High-temperature superconducting nanowires for photon detection," *Physica C*, vol. 509, pp. 16–21, 2015.

[108] R. Arpaia, D. Golubev, R. Baghdadi, R. Ciancio, G. Dražić, P. Orgiani, D. Montemurro, T. Bauch, and F. Lombardi, "Transport properties of ultrathin $YBa_2Cu_3O_{7-\delta}$ nanowires: A route to single-photon detection," *Phys. Rev. B*, vol. 96, p. 064525, 2017.

[109] R. Arpaia, E. Andersson, A. Kalaboukhov, E. Schröder, E. Trabaldo, R. Ciancio, G. Dražić, P. Orgiani, T. Bauch, and F. Lombardi, "Untwinned $YBa_2Cu_3O_{7-\delta}$ thin

films on MgO substrates: A platform to study strain effects on the local orders in cuprates," *Phys. Rev. Materials*, vol. 3, p. 114804, 2019.

[110] D. Schweitzer, T. Bollmeier, B. Stritzker, and B. Rauschenbach, "Twinning of $YBa_2Cu_3O_7$ thin films on different substrates," *Thin Solid Films*, vol. 280, pp. 147–151, 1996.

[111] R. K. Singh and D. Kumar, "Pulsed laser deposition and characterization of high-T_c $YBa_2Cu_3O_{7-x}$ superconducting thin films," *Mater. Sci. Eng. R Rep.*, vol. 22, pp. 113–185, 1998.

[112] R. Liang, P. Dosanjh, D. Bonn, D. Baar, J. Carolan, and W. Hardy, "Growth and properties of superconducting YBCO single crystals," *Physica C*, vol. 195, pp. 51–58, 1992.

[113] R. Arpaia, S. Nawaz, F. Lombardi, and T. Bauch, "Improved nanopatterning for YBCO nanowires approaching the depairing current," *IEEE Trans. Appl. Supercond.*, vol. 23, pp. 1101505–1101505, 2013.

[114] S. Nawaz, R. Arpaia, F. Lombardi, and T. Bauch, "Microwave response of superconducting $YBa_2Cu_3O_{7-\delta}$ nanowire bridges sustaining the critical depairing current: Evidence of josephson-like behavior," *Phys. Rev. Lett.*, vol. 110, p. 167004, 2013.

[115] E. Andersson, R. Arpaia, E. Trabaldo, T. Bauch, and F. Lombardi, "Fabrication and electrical transport characterization of high quality underdoped $YBa_2Cu_3O_{7-\delta}$ nanowires," *Supercond. Sci. Technol.*, vol. 33, p. 064002, 2020.

[116] S. Charpentier, R. Arpaia, J. Gaudet, D. Matte, R. Baghdadi, T. Löfwander, P. Fournier, T. Bauch, and F. Lombardi, "Hot spot formation in electron-doped PCCO nanobridges," *Phys. Rev. B*, vol. 94, p. 060503, 2016.

[117] D. Golubev, "Resistive state triggered by vortex entry in $YBa_2Cu_3O_{7-\delta}$ nanostructures," *Physica C*, vol. 506, pp. 165–168, 2014.

[118] D. Golubev, F. Lombardi, and T. Bauch, "Effect of heating on critical current of YBCO nanowires," *Physica C*, vol. 506, pp. 174–177, 2014.

[119] M. Henny, S. Oberholzer, C. Strunk, and C. Schönenberger, "1/3-shot-noise suppression in diffusive nanowires," *Phys. Rev. B*, vol. 59, p. 2871, 1999.

[120] R. S. Prasher and P. E. Phelan, "Review of thermal boundary resistance of high-temperature superconductors," *J. Supercond.*, vol. 10, pp. 473–484, 1997.

[121] M. Nahum, S. Verghese, P. Richards, and K. Char, "Thermal boundary resistance for $YBa_2Cu_3O_{7-\delta}$ films," *Appl. Phys. Lett.*, vol. 59, pp. 2034–2036, 1991.

[122] M. Kelkar, P. E. Phelan, and B. Gu, "Thermal boundary resistance for thin-film high-T_c superconductors at varying interfacial temperature drops," *Int. J. Heat Mass Transf.*, vol. 40, pp. 2637–2645, 1997.

[123] A. Sergeev, A. Semenov, P. Kouminov, V. Trifonov, I. Goghidze, B. Karasik, G. Gol'tsman, and E. Gershenzon, "Transparency of a $YBa_2Cu_3O_7$-film/substrate interface for thermal phonons measured by means of voltage response to radiation," *Phys. Rev. B*, vol. 49, p. 9091, 1994.

[124] S. Zeuner, H. Lengfellner, and W. Prettl, "Thermal boundary resistance and diffusivity for $YBa_2Cu_3O_{7-\delta}$ films," *Phys. Rev. B*, vol. 51, p. 11903, 1995.

[125] A. Sergeev, "Electronic kapitza conductance due to inelastic electron-boundary scattering," *Phys. Rev. B*, vol. 58, p. R10199, 1998.

[126] L. Shi, G. Huang, C. Lehane, D. Kim, H. S. Kwok, J. Swiatkiewicz, G. C. Xu, and P. Prasad, "Picosecond photoresponse in Y-Ba-Cu-O ultrathin films," *Phys. Rev. B*, vol. 48, p. 6550, 1993.

[127] G. Mirarchi, R. Arpaia, E. Wahlberg, T. Bauch, A. Kalaboukhov, S. Caprara, C. Di Castro, M. Grilli, F. Lombardi, and G. Seibold, "Tuning the ground state of cuprate high-critical-temperature superconducting thin films by nanofaceted substrates," *arXiv:2306.12335*, 2023.

A

Appendix A

This section guides through the (draft) theoretical framework for the development of the heat transport due to injected electrical power (Joules heating) for the YBCO nanowires, which attempts to include the effect of e-ph coupling [118, 119]. The main assumption is that the wire is in the steady state response ($\frac{\partial T}{\partial t} = 0$), just to simplify the physics at play. Since we want to identify how the electronic temperature (T_e) and phononic temperature (T_{ph}) are affected by the Joule heating power, the relations are derived using the boundary condition $P_{in}^{electrical} = P_{out}^{thermal}$. The temperature profile for the electronic and phononic systems can be expressed as

$$e: \quad -\frac{\partial}{\partial x}\left(\kappa_e \frac{\partial T_e}{\partial x}\right) = \sigma\frac{V^2}{L^2} - \sigma \cdot \Gamma_{e-ph}\left(\frac{k_b}{e}\right)^2\left(T_e^5 - T_{ph}^5\right) \tag{A.1}$$

$$ph: \quad -\frac{\partial}{\partial x}\left(\kappa_{ph} \frac{\partial T_{ph}}{\partial x}\right) = \sigma \cdot \Gamma_{e-ph}\left(\frac{k_b}{e}\right)^2\left(T_e^5 - T_{ph}^5\right) \; - \frac{G_{TH}^{int}}{t}\left(T_{ph} - T_{sub}\right). \tag{A.2}$$

The following is the explanation of the parameters. First, we have $\kappa_{e/ph}$ and σ which are the thermal and electrical conductivity of the YBCO. The term $\sigma\frac{V^2}{L^2}$ describes the dissipated power per unit volume (P_{vol}). Next, we have the e-ph coupling Γ_{e-ph} and the YBCO/substrate interface conductance (G_{TH}^{int}) which describes different mechanisms for heat transfer between the electron and phonon system and between the YBCO phonons and the substrate phonons, respectively. The interface conductivity is also related to the substrate temperature, denoted as T_{sub}. Finally, we have two structural parameters which are length (L) and thickness (t). It is noted that the e-ph coupling term in (A.1) is only valid for metallic systems, which typically is applicable for the temperature under 10K [119]. However, we do not know which functional dependence can be applied to the YBCO as there is still currently no report on this matter. In addition, the interface conductance term with T-linear dependency (A.2) is an empiric expression derived from experimental observations (e.g., see [122]).

Assuming that the electron and phonon temperature are in thermal equilibrium ($T_e = T_{ph} = T$),

$$-\frac{\partial}{\partial x}\left((\kappa_{el} + \kappa_{ph})\frac{\partial T}{\partial x}\right) = P_{vol} - \frac{G_{TH}^{int}}{t}\left(T_{ph} - T_{sub}\right) \tag{A.3}$$

When the length (L) of the nanowire is much longer than e-ph scattering (l_{e-ph}) and thermal relaxation (l_0) lengths ($L \gg l_{e-ph}, l_0$), the contributions from the thermal conductivity between the wire and electrodes can be ignored ($\frac{\partial T}{\partial x} = 0$). Then, we get

$$P_{vol} = \frac{G_{TH}^{int}}{t}\left(T_{ph} - T_{sub}\right) \tag{A.4}$$

which describes the temperature rise in YBCO due to the finite interface conductivity. For the general case ($T_e \neq T_{ph}$) we obtain in the long wire limit by setting $\frac{\partial T_e}{\partial x} = 0$ and $\frac{\partial T_e}{\partial x} = 0$ in equation (A.1) and (A.2), which yields

$$e: \quad 0 = P_{vol} - \sigma \cdot \Gamma_{e-ph} \left(\frac{k_b}{e}\right)^2 \left(T_e^5 - T_{ph}^5\right) \tag{A.5}$$

$$ph: \quad 0 = \sigma \cdot \Gamma_{e-ph} \left(\frac{k_b}{e}\right)^2 \left(T_e^5 - T_{ph}^5\right) - \frac{G_{TH}^{int}}{t} \left(T_{ph} - T_{sub}\right) \tag{A.6}$$

Then, we can subtract the electronic (A) with phononic (A.6) term to get

$$0 = P_{vol} - 2 \cdot \Gamma_{e-ph} \left(\frac{k_b}{e}\right)^2 \left(T_e^5 - T_{ph}^5\right) + \frac{G_{TH}^{int}}{t} \left(T_{ph} - T_{sub}\right). \tag{A.7}$$

Lastly, we remove the contribution from the interface conductance which results in

$$P_{vol} = \sigma \cdot \Gamma_{e-ph} \left(\frac{k_b}{e}\right)^2 \left(T_e^5 - T_{ph}^5\right) \tag{A.8}$$

which describes the power dissipation due to the e-ph scattering. Therefore, we have obtained the two coupled equations

$$e - ph: \quad P_{vol} = \sigma \cdot \Gamma_{e-ph} \left(\frac{k_b}{e}\right)^2 \left(T_e^5 - T_{ph}^5\right) \tag{A.9}$$

$$int: \quad P_{vol} = \frac{G_{TH}^{int}}{t} \left(T_{ph} - T_{sub}\right) \tag{A.10}$$

which describes how the power is dissipated through the YBCO nanowire. Firstly, the power is converted into heat due to Joule heating. The generated heat then dissipates firstly into the electronic system of the YBCO. Due to e-ph coupling, the heat from the electronic is dissipated into the phononic system. Lastly, the heat from the phononic system is dissipated into the substrate by interface scattering. Then, the relations for T_e and T_{ph} with applied power are

$$e - ph: \quad T_e = \left(T_{ph}^5 + \frac{1}{\sigma \cdot \Gamma_{e-ph} \left(\frac{k_b}{e}\right)^2} \cdot P_{vol}\right)^{1/5} \tag{A.11}$$

$$int: \quad T_{ph} = T_{sub} + \frac{t}{G_{TH}^{int}} \cdot P_{vol}. \tag{A.12}$$

The factor $\frac{1}{\sigma \cdot \Gamma_{e-ph} \left(\frac{k_b}{e}\right)^2}$ describes the contribution of e-ph coupling to the thermal resistance (R_{TH}^{e-ph}), while the factor $\frac{1}{G_{TH}^{int}}$ (or R_{TH}^{int}) describes the thermal resistance at the YBCO/substrate interface. It is noted that the unit for the R_{TH}^{e-ph} does not directly describe the thermal resistance of the e-ph scattering, but we will call the terms R_{TH} mainly for convenience. To get a better idea of how the heating effects are related to the dimension of the nanowires, we can multiply the equations (A.11) and (A.12) by the volume of the nanowire with ($Volume = L \cdot W \cdot t$),

$$e-ph: \quad P = \left(1/R_{TH}^{e-ph}\right)(L \cdot W \cdot t)\left(T_e^5 - T_{ph}^5\right) \tag{A.13}$$

$$int: \quad P = G_{TH}^{int}(L \cdot W)(T_{ph} - T_{sub}). \tag{A.14}$$

Which can be rearranged to take the same form as equations (A.11) and (A.12)

$$e-ph: \quad T_e = \left(T_{ph}^5 + \frac{R_{TH}^{e-ph}}{Volume} \cdot P\right)^{1/5} \tag{A.15}$$

$$int: \quad T_{ph} = T_{sub} + \frac{R_{TH}^{int}}{Area} \cdot P. \tag{A.16}$$

Equation (A.15) and (A.16) shows that the e-ph coupling depends on the whole volume of the nanowire, while the interface conductance only depends on the interface area ($Area = L \cdot W$). The effect of e-ph coupling is expected to be enhanced when reducing the thickness (t) of the nanowire without affecting the temperature rise due to interface conductivity. Then, the effect of e-ph should be more pronounced in the t=10 nm nanowires. Nevertheless, the thickness dependence measurements of the T(P) and total thermal conductivity are required to confirm the effect.

DEPARTMENT OF MICROTECHNOLOGY AND NANOSCIENCE
CHALMERS UNIVERSITY OF TECHNOLOGY
Gothenburg, Sweden
www.chalmers.se

CHALMERS
UNIVERSITY OF TECHNOLOGY